

**Iron oxide minerals in dust-source sediments from the Bodélé Depression, Chad:
Implications for radiative properties and Fe bioavailability of dust plumes from the
Sahara**

Bruce M. Moskowitz^{1*}, Richard L. Reynolds^{1,2}, Harland L. Goldstein², Thelma S. Berquó³,
Raymond F. Kokaly², and Charlie S. Bristow⁴

¹Institute for Rock Magnetism, Department of Earth Sciences, University of Minnesota,
Minneapolis, Minnesota, USA

²U.S. Geological Survey, Denver, Colorado, USA

³Department of Physics, Concordia College, Moorhead, Minnesota, USA

⁴School of Earth Sciences, Birkbeck College, University of London, Malet St., London WC1E
7HX, UK

*Corresponding author. Address: Department of Earth Sciences, University of Minnesota, 310
Pillsbury Dr. SE, Minneapolis, Minnesota 55455 United States. Tel. +1 612-624-1547; Email
address: bmosk@umn.edu

Keywords: dust; magnetic properties; goethite; hematite; nanoparticles; particulate matter

Abstract

Atmospheric mineral dust can influence climate and biogeochemical cycles. An important component of mineral dust is ferric oxide minerals (hematite and goethite) which have been shown to influence strongly the optical properties of dust plumes and thus affect the radiative forcing of global dust. Here we report on the iron mineralogy of dust-source samples from the Bodélé Depression (Chad, north-central Africa), which is estimated to be Earth's most prolific dust producer and may be a key contributor to the global radiative budget of the atmosphere as well as to long-range nutrient transport to the Amazon Basin. By using a combination of magnetic property measurements, Mössbauer spectroscopy, reflectance spectroscopy, chemical analysis, and scanning electron microscopy, we document the abundance and relative amounts of goethite, hematite, and magnetite in dust-source samples from the Bodélé Depression. The partition between hematite and goethite is important to know to improve models for the radiative effects of ferric oxide minerals in mineral dust aerosols. The combination of methods shows (1) the dominance of goethite over hematite in the source sediments, (2) the abundance and occurrences of their nanosize components, and (3) the ubiquity of magnetite, albeit in small amounts. Dominant goethite and subordinate hematite together compose about 2% of yellow-reddish dust-source sediments from the Bodélé Depression and contribute strongly to diminution of reflectance in bulk samples. These observations imply that dust plumes from the Bodélé Depression that are derived from goethite-dominated sediments strongly absorb solar radiation. The presence of ubiquitous magnetite (0.002-0.57 wt. %) is also noteworthy for its potentially higher solubility relative to ferric oxide and for its small sizes, including $PM_{<0.1\mu m}$. For all examined samples, the average iron apportionment is estimated at about 33% in ferric oxide minerals, 1.4 % in magnetite, and 65% in ferric silicates. Structural iron in clay minerals may account for much of the iron in the ferric silicates. We estimate that the mean ferric oxides flux exported from the Bodélé Depression is 0.9 Tg/yr with greater than 50% exported as ferric oxide nanoparticles ($<0.1\mu m$). The high surface-to-volume ratios of ferric oxide nanoparticles once entrained into dust plumes may facilitate increased atmospheric chemical and physical processing and affect iron solubility and bioavailability to marine and terrestrial ecosystems.

Keywords: Dust sources, Magnetic properties, Bodélé Depression, Goethite, Hematite, Nanoparticles

1. Introduction

The composition of particulate matter in atmospheric dust strongly influences the optical properties of dust plumes and thus partly controls the radiative forcing of global dust. Solar energy interacts with dust particles in several ways. For example, bright (white) dust from salt-crusts dry lakes can reflect sunlight, and many mineral types, such as quartz, can scatter sunlight. In most far-traveled dust today, moreover, absorption of solar energy by certain soil-derived ferric oxide minerals, such as hematite ($\alpha\text{Fe}_2\text{O}_3$) and goethite (αFeOOH), and by a class of carbonaceous, mostly anthropogenic particles known loosely as “black carbon” strongly influences radiative forcing (Sokolik and Toon, 1999; IPCC, 2007). Before industrialization and widespread forest-clearing by burning, the ferric oxide minerals were likely supremely important in controlling the climatic effects from dust aerosols through absorption of solar radiation.

The Bodélé Depression (north-central Africa) is Earth’s most prolific dust producer and may be key component to the global radiative budget of the atmosphere as well as to long-range nutrient transport to the Amazon rainforest (e.g., Prospero et al., 2002; Washington et al., 2003; Giles, 2005; Goudie and Middleton, 2006; Warren et al., 2007; Bristow et al., 2009, 2010; Hudson-Edwards et al., 2014; Yu et al., 2015). The Bodélé dust-source region consists mainly of diatomaceous lake beds overridden by dunes and other aeolian deposits (e.g., Warren et al., 2007; Bristow et al., 2009), which are driven by dominant northeasterly winds (Washington and Todd, 2005; Washington et al., 2006). These diatom-rich lake beds and their derived aeolian sediments are white and therefore very bright. As expected, dust from this central region appears as distinct white plumes, especially in transit over darker desert terrain directly to the southwest of the diatomaceous lake basin. These factors give the impression that dust from the central Bodélé is perhaps entirely diatomaceous. Field observations give a different impression: Much of the very fine grained aeolian sediment within the central, bright-surfaced Bodélé Depression contains sufficient amounts of ferric oxide to impart hues of light red, orange, pink and gray. At ground-level, blowing dust within the central Bodélé is characterized by pale ochre and light grey colors. None of this is surprising when considering the bigger dust-source region. The diatomaceous central Bodélé is surrounded by weathered, wind-eroded landscapes of much older substrates, including Paleozoic and Cretaceous sedimentary rocks as well as ferric-oxide bearing Tertiary continental sedimentary rocks and the surficial deposits produced from them (Kusnir, 1995; Mounkaila, 2006; Bristow et al., 2009). Dust from these areas show reddish hues in satellite retrievals, such as from MODIS (MODerate resolution Imaging Spectroradiometer), but with less contrast with underlying surfaces than the lighter colored dust plumes from the diatomaceous sources (Koren and Kaufman, 2004).

Measurements of physical properties were made on samples from the Bodélé Depression collected in 2005. One aim was to compare bulk sample radiative properties with the amount of iron oxide minerals. A measure of radiative property was obtained by direct measurement of reflectance spectra, and the concentrations of ferric oxide was obtained by magnetic techniques. We also determined

the type of ferric oxide mineral, whether primarily hematite ($\alpha\text{-Fe}_2\text{O}_3$) or goethite ($\alpha\text{-FeOOH}$), which are the two most common forms in desert soils and surfaces (hereafter collectively referred to as iron oxides or ferric oxides), and which have different optical properties. Reflectance spectroscopy can be used to identify different ferric oxide minerals (e.g., Clark et al., 2007), as can certain magnetic methods (Maher et al., 2004; Guyodo et al., 2006; Carter-Stiglitz et al., 2006; Liu et al., 2006; Maher, 2011). Mössbauer spectroscopy was also employed to identify with high specificity various iron phases, including amounts of hematite and goethite as well as the fraction that occur as nanoparticles, in a sample.

In the following, we address the following questions: What iron oxide minerals are present in Bodélé dust and in what amounts, and what are their effects, if any, on radiative properties of Bodélé dust? Answers to these questions would improve understanding about the influences of variable particulate composition on dust-plume reflectance and would improve radiative transfer modeling for Saharan dust. The characterization of iron oxide minerals in the Bodélé dust-source region may also shed light on iron phases as potential nutrients in downwind marine and terrestrial ecosystems.

2. Materials and Methods

2.1 Samples.

Surface sediment samples were collected from 15 locations within the Bodélé Depression during the 2005 Bodélé Dust Experiment (BoDEX; Washington et al., 2006). Site locations were selected that most likely represent dust sources (Fig. 1) and consisted of diatomaceous sands and lacustrine and fluvial-deltaic sediments. A list of sample locations along with a brief field description are given in Table 1 and field photographs of site locations are given in Hudson-Edwards et al. [2014]. Samples consisted of two types: (1) loose sediment and (2) large fragments of consolidated diatomite (here referred to as “peds”). Loose sediment samples were sieved to isolate three size fractions: (a) Less than $63\ \mu\text{m}$ (PM63; “fines”), the sizes most likely to be emitted as dust; (b) the size range between 63 and $125\ \mu\text{m}$ (“medium-grained”); and (c) size range between 125 and $2000\ \mu\text{m}$ (“coarse-grained”). Ped samples were cleaned gently to remove loose sediment that may have stuck to the ped. One ped sample was brushed more vigorously to remove a coating of loose sediment.

2.2 Reflectance spectroscopy

Reflectance spectra of samples were measured for identification of constituent phases and to determine average reflectance values. Average total reflectance (ATR) is average reflectance over the entire wavelength range (0.35 to $2.50\ \mu\text{m}$) and average visible reflectance (AVR) is average reflectance over the visible wavelengths (0.40 to $0.70\ \mu\text{m}$). Reflectance spectra were measured in the laboratory using an Analytical Spectral Devices (ASD) FieldSpec4 (FS4) standard resolution spectrometer, covering the wavelength range of 0.35 to $2.50\ \mu\text{m}$ in 2151 channels. A bi-directional reflectance measurement setup was used, with the light source and the fiber optic head of the spectrometer at fixed angles above the sample. With this setup, biconical reflectance factors were measured according to the nomenclature of Schaepmann-Strub et al. (2006), hereafter referred to as reflectance. For each sample, multiple

reflectance measurements were made relative to a Spectralon white reference panel (Labsphere, North Sutton, New Hampshire). The individual measurements were averaged and the average spectrum was converted to absolute reflectance using the USGS Processing Routines in IDL for Spectral Measurements (PRISM; Kokaly, 2011); for details on the conversion process, see the methods section in Kokaly and Skidmore (2015). We identified ferric oxide and some clay minerals by analyzing reflectance spectra using the Material Identification and Characterization Algorithm (MICA), a module of the PRISM software system (Kokaly, 2011), which uses continuum removal to isolate diagnostic absorption features and linear regression to compare spectral features. In this way, the spectra of Bodélé samples are compared with reference spectra of minerals and other materials (Clark et al., 2007). In this study, we are interested in the iron-bearing minerals with electronic absorption features centered primarily in the visible and near-infrared wavelengths (0.4 to 1.0 μm). The MICA analysis computes a fit value, ranging from 0 to 1, between the sample spectrum and each reference material (Kokaly, 2011), with “best fit” determined by the highest fit value.

2.3 Magnetic Methods

Magnetic properties as a function of applied field, temperature, and frequency provide information about the types, amounts, and sizes of magnetic iron-oxide minerals and can help to distinguish between ferrimagnetic minerals, such as (titano)magnetite and maghemite, antiferromagnetic ferric oxide minerals, such as hematite and goethite, and superparamagnetic nanophase ($< 30 \text{ nm}$) particles (e.g., Evans and Heller, 2003; Maher, 2011). Magnetic measurements between 10 K and 300 K are particularly useful because magnetite undergoes a structural phase transition, called the Verwey transition, at $T_v=120 \text{ K}$, whereas hematite undergoes a magnetic transition, called the Morin transition, at $T_m=250 \text{ K}$ [e.g., Dunlop and Özdemir, 1997; Özdemir et al., 2008]. Both transitions produce characteristic remanence and susceptibility behavior during thermal cycling between 300 and 10 K that can be diagnostic indicators for these two phases. Both transition temperatures are also affected by small amounts of cation impurities, moderate degrees of non-stoichiometry, and nanometric effects, which can lower and broaden the transition temperatures or suppress them entirely, but which also provide additional diagnostic indicators of these departures from ideal behavior.

Room-temperature isothermal remanent magnetization (IRM) on sized-fractions (PM63, 63-125 μm , 125-2000 μm) were measured at the U.S. Geological Survey (Denver, CO, USA) using an Agico JR-5A (90-Hz) spinner magnetometer. A more extensive set of magnetic measurements on a smaller subset of PM63 (CH2, CH8, CH11, CH23, CH24, CH39, CH80, and CH81) and 125-200 μm (CH8, CH11, CH80, CH81) samples were measured at Institute for Rock Magnetism (University of Minnesota, USA). Samples for magnetic analysis were prepared by either packing approximately 200 mg of bulk sediment into #4 gelatin capsules (Institute for Rock Magnetism) or approximately 1000-4000 mg of bulk sediment into small plastic boxes (U.S. Geological Survey). All sample measurements were normalized by mass.

Room-temperature hysteresis loops and dc backfield remanence curves were measured on a Princeton Measurements vibrating sample magnetometer using a maximum field of 1.0 T. Hysteresis parameters

(saturation magnetization, M_s ; saturation remanence, M_r ; coercivity, H_c ; and high-field susceptibility, χ_{hf}) were determined from loops after high-field slope correction (Jackson and Solheid, 2010). The shape of the loop was quantified using the shape parameter (σ_{hys}) of Fabian (2003). The weight percent magnetite was determined from the room-temperature bulk saturation magnetization values and the known value for pure magnetite ($M_s=92 \text{ Am}^2/\text{kg}$) as: $\text{wt\% magnetite} = 100\% \times M_s/(92 \text{ Am}^2/\text{kg})$.

Coercivity of remanence (H_{cr}), hard isothermal remanent magnetization (HIRM) and the S_{300} -ratio were determined from dc backfield remanence curves obtained by demagnetizing a saturation IRM (SIRM) acquired in 1.0 T in a stepwise manner in increasing back fields to -1.0 T. For the USGS series of measurements, SIRM was acquired in a maximum field of 1.2 T and then at a backfield of -0.3T. The hard isothermal remanent magnetization (HIRM) values and the S_{300} -ratio were calculated using the following definitions: $\text{HIRM} = 0.5 \times (\text{SIRM} + \text{IRM}_{-0.3T})$ and $S_{300} = (\text{IRM}_{-0.3T})/\text{SIRM}$ (King and Channel, 1991).

SIRM and M_s are mainly controlled by the amount of magnetite or maghemite when present, even when in small amounts. Since magnetite and maghemite are usually completely saturated above 0.3 T, HIRM is a measure of the amount of high-coercivity, antiferromagnetic phases (hematite and goethite) and the S_{300} -ratio is a measure of the relative amounts of low-coercivity (magnetite/maghemite) to high-coercivity (hematite/goethite) phases. However, since goethite is extremely hard to magnetize at room temperature in fields below 2.0 T (Maher et al., 2004; Rochette et al., 2005) it may contribute a negligible amount to HIRM or the S_{300} -ratio value even though it may be the abundant phase. Furthermore, depending on particle sizes and cation impurity, the magnetic ordering temperature for goethite may be below room-temperature and thus be invisible to remanence measurements at room-temperature [Liu et al., 2006].

Low-temperature remanent magnetization and ac susceptibility (χ) were measured using a Quantum Design Magnetic Properties Measurement System. Low-temperature IRM was imparted to samples in 2.5 T field at 10 K. Prior to imparting the IRM at 10 K, samples were pretreated by either cooling to 10 K in 2.5 T (in-field cooling, FC) or in zero-field (zero-field cooling, ZFC). ZFC and FC curves were measured on warming in approximately zero field to 300 K in 5 K increments (residual field is approximately 100 μT). Samples were also given a SIRM in a field of 2.5 T at 300 K (RTSIRM) and magnetization was measured during cooling to 10 K and warming back to 300 K in zero field at 5 K increments. To test for the presence of nanophase, superparamagnetic particles, in-phase (χ') and quadrature (χ'') magnetic susceptibility was measured in an ac field with peak amplitude of 0.3 mT at 4 or 5 different frequencies between 1 and 1000 Hz on warming from 10 to 300 K. Frequency dependent susceptibility (χ_{fd}) was calculated from the slope of the best-fit line to the χ' -log (frequency) curve at constant temperature.

To evaluate the relative contributions of goethite and hematite to the total remanence, several additional low-temperature cycling runs were measured following procedures in Guyodo et al. (2006) and Carter-Stiglitz et al. (2006). These additional steps are designed to minimize the contribution from

strongly magnetic minerals like magnetite and maghemite, which can dominate the FC, ZFC, and RTSIRM magnetizations, and target weakly magnetic, antiferromagnetic minerals with high coercivities like goethite and hematite. The Carter-Guyodo method makes use of the low coercivity of magnetite and maghemite compared to hematite and goethite plus the difference in LT magnetic behavior between hematite and goethite [Rochette and Fillion, 1989; Maher et al., 2004; Liu et al., 2006]. Our experimental protocol is described in Reynolds et al. [2014a, b]. The remanence ratio, $R_{LT} = \text{IRM}(10\text{K})/\text{IRM}(300\text{K})$, was calculated from the remanence cooling segment of the Carter-Guyodo method after alternating-field demagnetization at 300 K, where IRM (10 K) and IRM (300 K) are remanence values measured at 10 K and 300 K, respectively (Liu et al., 2006). In pure minerals, goethite can have R_{LT} ratios greater than 2.0 (Guyodo et al., 2003; Liu et al., 2006), whereas magnetite and hematite have R_{LT} ratios near 1.0 or less.

2.4 Mössbauer spectroscopy

Mössbauer spectra were measured at the Institute for Rock Magnetism (University of Minnesota, USA) on bulk PM63 samples CH02, CH24, CH62, and CH39 to further characterize iron oxide mineralogy and to detect the presence of nanophase ferric oxides. Measurements were made at 300 K and 4.2 K using a constant-acceleration spectrometer equipped with a Nitrogen shielded Helium dewar. Spectra were collected in transmission geometry with a $^{57}\text{Co}/\text{Rh}$ source. An alpha-Fe foil at room temperature was used to calibrate isomer shifts and velocity scale. Mössbauer spectra were fit using the NORMOS program (Brand, 1987) providing estimates for the hyperfine field (B_{hf}), isomer shift (IS), and quadrupole splitting (QS) for each subspectra. Magnetically split sextet subspectra were fit using a distribution of hyperfine-fields (HFD). Uncertainties for Mössbauer parameters are ± 0.01 mm/s for IS and QS, ± 0.1 T for B_{hf} , and $\pm 5\%$ for spectral area.

2.5 Scanning Electron Microscopy

Several sediment samples were examined at resolutions above 9 nm using Scanning Electron Microscopy (SEM; FEI Quanta) methods, with secondary and backscatter electron detectors and an attached energy dispersion X-ray system (EDS). Samples were dispersed in isopropyl alcohol, transferred to polished carbon planchets, and carbon coated prior to examination.

2.6 Major element analysis

Major, minor, and trace elements were determined using quadruple inductively coupled plasma and ICP–mass spectrometry (ICP–MS, Wolf and Adams, 2015) following a four-acid digestion (Briggs and Meier, 2002).

3.0 Results

3.1. Reflectance Spectroscopy

In some samples, average visible reflectances are less in the finer-grained fraction than in the coarse-grained fraction (Fig. 2). The presence of goethite is confirmed in these fine-grained samples as discussed below (Table 2). However, for all samples the average total reflectance decreases with

increasing grain-size (Fig. S1 and Table S1 in Supplementary Data). This relation is primarily related to the presence of gray rock fragments that are most abundant in the coarse fractions and absent in the fines.

The best-fitting routine matched a goethite standard to seven samples that all had a yellow-red hue, commonly 7.5YR 6/3. Hematite was a secondary match in six of these samples (Table 2). The goethite-bearing samples have similar reflectance values across the visible part of the spectrum regardless of particle size. Visible reflectance values for samples containing iron oxides are overall almost 50 percent lower than those values for samples in which no iron oxide was identified. A fragment of diatomite (CH23-ped) that had been stained yellow by goethite-bearing fines in a collection bag had a reflectance value close to that of the fines. Gentle brushing of a companion diatomite fragment (CH23-ped B) produced a white surface, increased reflectance, and removed any trace of goethite (Table S1 in Supplementary Data).

3.2 Room Temperature Magnetic Properties: *HIRM and SIRM*

Mass specific magnetization (HIRM, SIRM) was found to vary over almost three orders of magnitude with the highest values represented by sample CH39 (silty Angamma Delta sediment) and the lowest value by diatomite sample CH50. There was also a grain-size dependent effect with the highest magnetization values occurring in the PM63 sized fraction (Fig. 3). Sample CH39 stands out as anomalous in terms of its intensity of magnetization as was noted by Oldfield et al. [2014]. Excluding CH39 for the moment, the remaining samples display a bimodal distribution separating into a high magnetization (HM) group (n=8, CH02-CH11, CH77-CH82) and a low magnetization (LM) group (n=6, CH23-CH26, CH50, CH62). The largest differences in magnetization between the two groups occur within the PM63 fraction (Fig. 3), indicating a significant difference in both the ferric iron oxide and magnetite concentrations between the two groups of samples. In the coarsest size fraction (125-2000 μm), however, the magnetization contrast all but disappeared.

Amounts of magnetic ferric oxide minerals estimated from HIRM show negative correspondence with average visible reflectance for all three sized fractions (Fig. 4). This correspondence was defined by CH50 at one end with very low ferric oxide content and high average visible reflectance, and by CH39 with higher ferric oxide amounts and lower reflectance. Correlation coefficients (r) and their level of significance (p) are: PM63 ($r=-0.81$, $p=0.001$), 63-125 μm ($r=-0.63$, $p=0.013$), and 125-2000 μm ($r=-0.58$, $p=0.031$). Estimates for magnetite concentration from SIRM and average visible reflectance values in these samples showed a similar pattern. Even without the anomalously high magnetization in CH39, the negative correlation persisted. However, the coarse fraction shows the weakest correlation between HIRM and reflectance and no significant correlation with SIRM. Similar correlations between HIRM and reflectance were found for dust samples associated with the Red Dawn dust storm in eastern Australia (Reynolds et al., 2014a) and dust-on-snow and dust source sediments from Utah, USA (Reynolds et al., 2014b).

3.3 Room Temperature Magnetic Properties: *Hysteresis Loops*

Hysteresis loops were measured for nine PM63 samples and provided additional information about particle sizes and concentration of magnetic phases (Fig. S2 and Table S2 in Supplementary Data). In all cases the loops have a positive high field slope (χ_{hf}) due to the strong influence of paramagnetic or antiferromagnetic phases, and closure occurs by 500 mT characteristic of ferrimagnetic phases like magnetite. Some loops have shape factors, $\sigma_{hys} > 0.2$, producing a slight constriction near the origin and indicating a mixture of low- and high-coercivity phases representing either mixtures of different minerals (magnetite/maghemite and hematite/goethite) or mixtures of different particle sizes in a single mineral (microcrystalline and nanometric) (Tauxe et al., 1996; Roberts et al., 1995; Dunlop 2002a, b).

The concentration of all iron oxide minerals is reflected by values of saturation magnetization (M_s), but is primarily generated by ferrimagnetic minerals with high intrinsic M_s (e.g., magnetite or maghemite). Assuming that M_s at room temperature is dominated by magnetite, the weight percentages of magnetite range from 0.002% to 0.57% (Fig. 5), but show a similar bimodal pattern in terms of the HM and LM samples groups as HIRM and SIRM. Saturation magnetization clearly shows the anomalous magnetic characteristics of sample CH39, which has more than 10 times the amount of magnetite (0.57 wt %) than any of the other BD samples measured (Table S2 in Supplementary Data). Sample CH39 is a silty sand collected from Angamma Delta and closest of all samples to the Tibesti volcanics. It is unlike the rest of the sample suite that consists of dune sands and diatomite. Therefore, it is not surprising that CH39 is unique in this suite with relatively high amounts of magnetite.

Although the concentration of magnetite varied greatly among the samples, hysteresis ratios, M_r/M_s , H_{cr}/H_c that are primarily sensitive to magnetic particle-size variations in the ferrimagnetic fraction, were mostly similar (Fig. 6; Day plot). The distribution of points on the Day plot display little variation and plot within a narrow belt near a theoretical binary mixing lines for single domain (fine-grained SD, $< 0.1 \mu m$) and multidomain (coarse grained MD, $> 10 \mu m$) magnetites but slightly offset towards the SD + superparamagnetic (SP) field of the diagram (Day et al., 1977; Dunlop 2002a, b). Admixtures of superparamagnetic particles would be consistent with the positive loop shape factors (σ_{hys}) for PM63 samples that plot farthest to the right of the SD-MD mixing field. Although associating a given data set to binary mixing curves on the Day plot is nonunique (Heslop and Roberts, 2012), the essential point is the similarity in the hysteresis ratios indicate a similar magnetite particle-size distribution across the sample set independent of the sized fraction and despite changes in concentration. The only exception was the outlier sample CH23, which was weakly magnetic resulting in a ferrimagnetic loop with a low signal/noise ratio and greater uncertainties in the derived hysteresis ratios.

3.4 Low-Temperature Magnetic Properties: FC, ZFC, and RTSIRM

Low temperature remanence (FC, ZFC, and RTSIRM) was measured for nine PM63 samples. The most visible feature of the FC and ZFC curves for the sample set was the exponential decay of remanence on warming from 10 K with as much as 90% of the initial remanence erased by 300 K (Fig. 7). This type of behavior is a hallmark of progressive thermal unblocking of superparamagnetic nanoparticles upon warming and implies that 90% of the magnetic phase responsible for the low-

temperature remanence is in the SP state at 300 K. Sample CH39, with a smaller decrease in remanence with warming, was the only sample that showed a slight change in slope near 120 K associated with the Verwey transition in magnetite. However, the presence of magnetite in the other samples was confirmed from the complementary RTSIRM experiment, which measures a remanence acquired at room temperature during cooling to 10 K. In this case, the superparamagnetic fraction, which is blocked and magnetized at 10 K during the FC/ZFC runs, does not contribute to the remanence acquired at 300 K. Here a more noticeable but small drop in remanence on cooling near 110-120 K was observed for most samples (Fig. S3 in Supplementary Data). Except for CH39, the magnetite transition was all weakly expressed and coupled with RTSIRM curves exhibiting a steady increase in remanence on cooling between 300 and 10 K that was nearly reversible on warming back to 300 K. The blurred Verwey transitions and a hump-shaped warming and cooling RTSIRM curves observed for CH39 indicate the magnetite is partially oxidized or mixed with maghemite [Özdemir and Dunlop, 2010]. No apparent Morin transitions ($T_m=263$ K), a unique signature for pure hematite, were observed in any of the RTSIRM thermal cycles. In addition, no magnetic signatures for goethite compositions with sufficiently high cation substitution (e.g., Al) to lower their Néel temperature below 300 K were observed on any of the FC and ZFC curves. Such cation loading would likely have produced a small drop in remanence between 200 and 300 K. For example, the observations indicate that if Al substitution is present in goethite it must be less than approximately 14 mole % Al [e.g., Liu et al., 2006].

A small but persistent separation between the FC and ZFC curves on warming (with $FC > ZFC$) was observed that gradually decreased as the curves merged together near 300 K (Fig. S4 in Supplementary Data). The offsets were more noticeable for the HM sample group. Large FC-ZFC offsets are typically seen for goethite [Guyodo et al., 2006, Carter-Stiglitz et al., 2006], and much smaller ones in multi-domain ($> 1 \mu m$), partially oxidized, magnetite [Smirnov and Tarduno, 2000]. Both phases probably contribute to the FC/ZFC behavior, but because of the very large differences in the intrinsic saturation magnetization between magnetite/maghemite and goethite, the former dominates in these series of measurements. This does not mean, however, that there is little goethite in the samples. In the next section, the goethite and hematite contributions can be identified and quantified using additional low-temperature magnetization experiments.

3.5 Low-Temperature Magnetic Properties: Goethite and Hematite

The Carter-Guyodo method, which effectively removes the strong magnetite component from the remanence signal by alternating field demagnetization, is designed to target the weakly magnetic antiferromagnetic phases (goethite and hematite) and allow their remanence contributions to the total magnetization to be quantified. The resulting remanence curves display two types of behavior which divide along the grouping of samples with high or low magnetization (Fig. 8). Goethite was identified in all samples by a reversible monotonic increase in remanence on cooling between 300 and 10 K [Rochette and Filton, 1989] with R_{LT} ratios greater than 2 (Fig. S5 in Supplementary Data). This type of behavior was observed in the RTSIRM experiments but with lower R_{LT} ratios because the goethite was not fully

magnetized as well as the additional magnetite contribution. In the HM group a non-reversible loss of remanence was observed near 350 K (Fig. 8a) corresponding to a Néel temperature slightly below that for pure, bulk goethite ($T_N=393$ K) and consistent with poorly crystalline or Al-substituted goethite (Liu et al., 2006). Conversely, in the LM group, no such marked transition occurred and only a small amount of irreversibility in remanence after heating to 400 K (Fig. 8b) was observed. It is puzzling why the Néel temperature was not observed for some of these samples which otherwise displayed the characteristic low-temperature cooling behavior of goethite ($R_{LT} > 2$). Similar behavior was observed in marine sediments from the Bengal Fan and was attributed to magnetic interaction between goethite and hematite in intimate contact allowing the goethite to be remagnetized by the hematite after cooling below the Néel temperature, even in zero field [Abrajevitch et al., 2009].

The other magnetic phase observed in Fig. 8 is the component that resisted alternating-field demagnetization to 0.2 T and thermal demagnetization to 400 K (a temperature above T_N for goethite). We interpret this component as hematite on the basis of its magnetization behavior and by its identification by Mössbauer spectroscopy (CH02, CH39) and reflectance spectroscopy (CH02, CH08, CH09, CH11, CH77, and CH82), even in the absence of an observed Morin transition in any of the samples. It is not unusual for the Morin transition to be suppressed in natural hematite due to poor crystallinity, cation-substitution, or nanoparticle effects (Vandenberghe et al., 2001; Maher et al., 2004; Özdemir et al., 2008; Jiang et al., 2014).

The individual contributions to the total remanent magnetization at 300 K for magnetite, hematite, and goethite can now be determined from results like those shown in Fig. 8 (Table S3 in Supplementary data), where the magnetite contribution was determined from the amount of magnetization removed by AF demagnetization. Magnetite dominates the remanent magnetization contributing more than 60% to the total (Fig. 9). Because the intrinsic magnetization of magnetite is more than 200 times higher than for hematite or goethite, a small amount of magnetite can easily dominate the remanent magnetization, even though hematite or goethite may be volumetrically dominant. Note that the relative contribution of magnetite in CH23, CH24, and CH62 (80-90%, LM group) is higher than in samples CH2, CH8, CH11, CH80, and CH81 (60-70%, HM group), even though in the former the wt% magnetite is 3-6 times less than in the latter (Fig. 5). In terms of the total ferric oxide contributions in the two groups, goethite and hematite combine to form approximately 40% of the remanence in the HM group but only 13% in the LM group. Individually, hematite contributes about equal amounts of 6-14% to the remanence, while goethite contributes significantly more (~16% vs. 2%) in the HM group (Fig. 9). This is consistent with the reflectance data for HM samples that showed that relative to goethite, hematite was the subordinate phase. A small fraction of hematite may also be partially demagnetized in 0.2 T AF during the first part of the Carter-Guyodo method, thereby underestimating the hematite contribution [Maher et al., 2004].

3.6 Low Temperature Magnetic Properties: Magnetic Susceptibility

The temperature dependence of ac susceptibility was measured at variable frequencies to identify potential contributions of superparamagnetic nanoparticles. Due to the low intrinsic susceptibilities for

hematite and goethite (e.g., Evans and Heller, 2003), susceptibility is primarily sensitive to paramagnetic or ferrimagnetic minerals when they occur in sufficient concentration to mask the effects of hematite or goethite. This effect seems to be the case for the Bodélé samples (Fig. S6 in Supplementary Data). The LM group shows paramagnetic behavior ($\chi \propto 1/T$) with a decrease in χ with increasing temperature and little frequency dependence. Superimposed on a paramagnetic background, in contrast, the HM group shows frequency dependence with non-zero quadrature susceptibility over the whole temperature range indicating a broad size distribution of magnetite nanoparticles (e.g. Worm, 1998). The $\chi'(T)$ curves do not show any indications of the Verwey or Morin transitions in agreement with the low-temperature magnetization results. In-phase susceptibility reaches a plateau or maxima near 30-50 K in the same temperature range where FC/ZFC remanence decays by approximately 50%. Besides magnetite, nanogoethite must also be responsible for some fraction of the observed frequency dependence at low temperatures. At room temperature, frequency dependent susceptibility is higher in the HM group ($\chi_{fd} = 5.9\text{-}9.2 \times 10^{-9} \text{ m}^3/\text{kg}$) than in the LM group ($\chi_{fd} = 0.4\text{-}2.1 \times 10^{-9} \text{ m}^3/\text{kg}$), indicating an enhancement of superparamagnetic grains in the HM samples. Except for CH39, low-field susceptibility is low ($\chi_{lf} < 4 \times 10^{-7} \text{ m}^3/\text{kg}$) due to the overall low abundance of ferrimagnetic minerals in all samples (Table S2 in Supplementary data).

3.7. Mössbauer Spectroscopy

Mössbauer spectra were measured at 300 K and 4.2 K for CH02, CH24, CH39 and CH62 (Fig. S7 in Supplementary Data). The RT spectra for all four samples were dominated by a paramagnetic doublet together with a smaller magnetically split sextet in CH02 and CH39 (Table S4 in Supplementary Data). The isomer shift (IS~0.5 mm/s) and quadrupole splitting (QS~0.55 mm/s) for the main doublet are consistent with octahedral Fe(III). Spectra for CH39 also contain a small Fe(II) doublet corresponding to 12% of the total spectral area. Possible candidate minerals for the paramagnetic doublets are kaolinite, illite, and smectite, which were all identified independently by reflectance spectroscopy. However, broadened resonant peaks of the paramagnetic Fe(III) and Fe(II) doublets likely represent several components with overlapping doublets with similar IS and QS values, such as phyllosilicates and nanophase iron oxides, and thus preclude firm identification of mineral phases (e.g., Dyar et al., 2006). In contrast, the hyperfine field (B_{hf}) values of 50.6 (CH02) and 49.8 (CH39) for the sextet component were consistent with hematite, with possible minor Al cation substitution (e.g., Vandenberghe et al., 2001; Morris et al., 1992). In both samples the doublet subspectra represented about 80% of the total Fe with hematite accounting for the other 20%.

Because all iron oxides possess magnetically split sextets at 4.2 K, additional information concerning mineralogy and particle sizes can be obtained. Mössbauer spectrum at 4.2 K for CH02 was composed of two magnetically split sextets and one doublet. In addition to the hematite sextet with $B_{hf} = 52.8 \text{ T}$ and $QS = -0.19$, a second sextet was resolved with $B_{hf} = 49.5 \text{ T}$ and $QS = -0.26 \text{ mm/s}$ that accords with previous studies for poorly crystallized and/or Al-substituted goethite (Fig. S7b in Supplementary Data). Identification of this component as goethite was also confirmed by reflectance spectroscopy. The B_{hf}

value for hematite was slightly diminished from its value for chemically pure, well-crystallized hematite. More revealing, the QS value was still negative at 4.2 K consistent with that expected for the hematite failing to undergo the Morin transition [Vandenberghe et al., 1990]. Similar to the reduction in B_{hf} , the suppression of the Morin transition can be produced by small particle sizes (< 50 nm), poor crystallinity, and/or cation substitution. Similar results were observed for CH39. The MB results are in agreement with low-temperature magnetometry, which also failed to detect the Morin transition in CH02 or CH39 as well as in all the other samples. In contrast to spectra for sample CH02 and CH39, those for samples CH24 and CH62 remained doublets and did not show any magnetic ordering at 4.2 K. Reflectance spectroscopy also failed to detect any Fe oxides in these two samples. These results indicated that the hematite/goethite concentrations in CH24 and CH62 were below the detection limits for MB and reflectance spectroscopy in view of their detection by low-temperature magnetometry, although in much lower amounts than in CH02.

The fact that the sextet associated with goethite in CH02 and CH39 was found at 4.2 K but not at 300 K indicated complete magnetic order for goethite only at very low temperatures and superparamagnetism at 300 K. This type of behavior occurs in nanogoethite when particle sizes are less than ~ 20 nm [Vandenberghe et al., 1990; van der Zee et al., 2003]. Unlike the RT spectra for CH02, the doublet subspectral area was diminished to account for 39% of the total Fe in the sample, whereas hematite and goethite accounted for 24% and 37%, respectively. The increase in the spectral area for hematite (from 19% to 24%) at 4.2K indicated that a fraction of the hematite was also ultrafine grained (less than about 50 nm and superparamagnetic at 300 K). The results for CH39 followed a similar pattern with temperature but with a greater fraction of Fe in paramagnetic phases (62%) and with more hematite (24%) than goethite (14%).

The increase in the goethite and hematite subspectral areas at the expense of the doublet area at 4.2 K confirmed that part of the RT doublet must be attributed to nanophase goethite and hematite. Even though MB indicated only nanogoethite, the magnetization experiments also indicated that some fraction of the goethite particle-size distribution carried remanence at 300 K, and hence had particle sizes with blocking temperatures above 300 K and long relaxation times. This fraction would have produced a sextet superposed with the SP doublet at 300 K but it must have been a sufficiently small volume fraction that the sextet cannot be resolved. Furthermore, nanoparticles of antiferromagnetic minerals like goethite may have small uncompensated magnetic moments due to surface or volume defects, enhancing the magnetization over bulk values [e.g., Guyodo et al., 2006]. Therefore, remanent magnetization data may not be directly comparable to Mössbauer data.

3.8 Scanning electron microscopy (SEM) observations

Many occurrences of iron were documented in samples CH77 (hand-sampled blown dust and sand), CH82 (laminated diatomite), and CH39 (Angamma Delta silty sand), all in associations with other particles and aggregates of particles. In all samples, discrete iron oxide particles occur as small (sub-micrometer) particulates on surfaces of larger particles, many of which are smectite or aggregates of

illite-smectite. In one example, iron oxide particles, having thicknesses of a few tens of nm, partly envelop a smectite clay particle about 300 nm across (Fig. 10). Structural iron was detected within clay minerals, including those that coat sulfate particles, which included barite (BaSO_4) in all samples, thenardite (Na_2SO_4) in sample CH82, and gypsum ($\text{CaSO}_4 \cdot 2\text{H}_2\text{O}$) in samples CH39 and CH82. All samples contained nano-size titanium dioxide (probably anatase or rutile), and rock-derived particles of Fe-Ti oxide minerals about 50-100 nm across as the most common occurrence for iron in sample CH39. Such Fe-Ti oxides are likely ilmenite that can be typically associated with Ti-bearing magnetite particles and corresponding to the relatively high concentration of magnetite in this sample (high M_s and IRM values, Table S2 and S3 in Supplemental data). Relevant to observations of Fe occurrences as potential nutrients, another notable feature in sample CH77 was the presence of iron oxide in mineral aggregates that contain apatite ($\text{Ca}_5(\text{PO}_4)_3(\text{F}, \text{Cl}, \text{OH})$) particles of varying sub-micrometer sizes as small as about 100 nm across (Fig. S8 in Supplementary Data). In this sample, apatite was also associated with phosphorus-rich organic carbon.

4.0 Discussion

4.1 Forms and occurrences of ferric oxide minerals.

In reflectance measurements with best-fit matching to standards, goethite was found to be the dominant ferric oxide in our samples, suggesting the importance of goethite across Bodélé dust sources. Details of ferric oxide mineralogy from magnetic properties and Mössbauer spectroscopy confirm that both goethite and hematite are present in amounts totaling about 2 wt%, with dominant goethite as explained in the following. Both ferric oxides are impure and probably contain some cation substitution, such as Al. A significant fraction of the ferric oxide occurs as superparamagnetic nanoparticles, whose presence is documented from the absence of Morin Transition (hematite) in low-temperature demagnetization curves, differences in low-temperature and high-temperature MB spectra (goethite and hematite), and frequency-dependent susceptibility over a wide temperature range for magnetite.

Examination of BD particles using SEM-EDS methods reveals the presence of individual particles of nanosize ferric oxide minerals, commonly within or coating clay minerals. Such occurrences have been observed in far-traveled dust in Australia (Reynolds et al., 2014a) and from Asia (Jeong and Nousiainen, 2014). These observations complement experimental results by Baddock et al. (2013) that inferred production of iron-rich nanoparticles from clay coatings on larger particles by abrasion from saltation during dust-producing wind events.

Total iron concentration is the highest for CH39 (5.4%) but decreases to 1.5 to 3.7% for the other PM63 samples. We use the results from CH02, which has the most complete set of measurements (Fe concentration (1.8%), magnetic analysis (for magnetite), and MB results at 4.2 K), to calculate the Fe partitioning among hematite, goethite, silicates, and magnetic nanophases in the HM and LM sample groups. CH02 contains 1.1 wt% goethite (37% of total Fe) and 0.6 wt% hematite (24% of total Fe). The sum of hematite and goethite accounts for 62% of the total Fe with 69% of the ferric oxides in the form of nanoparticles, primarily nanogoethite. Magnetite accounts for about 1.4 % of the total Fe (or 0.035

wt% magnetite), some of which also occurs in nanoparticles. We do not know whether the nanosize magnetite occurs as individual particles or as aggregated particles or inclusions. The remaining iron (~37%) is in paramagnetic phases, which are ascribed to structural iron within ferric silicate minerals (Table S3 in Supplementary data).

Our determination of the Fe fraction ratio of goethite to hematite for CH02 (Gt/Ht~1.54) compares favorably to results obtained using X-ray absorption spectroscopy by Formenti et al [2014a] for dust emitted from the Bodélé Depression but collected approximately 1800 km west at a ground-based site in Banizoumbou, Niger (Gt/Ht=1.31-1.67). Less agreement was found for the percentage of total Fe occurring as ferric oxide (goethite and hematite). Our surface sediment sample contains significantly more Fe in ferric oxides (61%) than the values obtained for the dust (36-40%), although some of this difference likely reflects local source heterogeneity and the mixing of dust across the dust-source region. Interestingly, when an independent chemical extraction method (Citrate-Bicarbonate-Dithionite or CBD) was used on one of the Bodélé dust samples a higher fraction of Fe as ferric oxides (52%) was found (Formenti et al., 2014a).

If we assume that the entire magnetization for hematite (M_{Ht}) at room temperature for CH02 (derived from the Carter-Guyodo method) is saturated and carried by SD grains with a bulk saturation remanence of $0.2 \text{ Am}^2/\text{kg}$, then the hematite concentration is ~0.3 wt%, basically in agreement with the Mössbauer data at 300 K (0.6 wt%). The MB results should give a higher weight percentage because it includes additional blocked superparamagnetic hematite particles that do not contribute to the remanence at 300 K. The SD assumption is reasonable because SD behavior in hematite occurs over a wide grain size interval (i.e., 0.030 to $10 \mu\text{m}$, Özdemir and Dunlop, 2014). Applying the same assumption for the rest of the sample set, there is ~0.2-0.3% hematite by mass in the HM group decreasing to ~0.02% for the LM group.

Doing the same type of analysis for the goethite contribution is more problematic for two reasons. First, the intrinsic magnetization parameters (saturation magnetization and remanence) for goethite are more structure sensitive and, hence, more highly variable in nature than hematite. Second, most of the goethite is superparamagnetic at room-temperature and will not contribute to the remanent magnetization, and thereby underestimating its abundance. Given these limitations, the nearly equal values for the hematite (M_{Ht}) and goethite (M_{Gt}) remanent magnetizations at room temperature in the HM group (i.e., M_{Gt}/M_{Ht} ratios ~1.0-1.4) indicate approximately similar mixtures of non SP hematite and goethite. Overall the goethite concentration must be greater than the hematite concentration when the SP fraction is taken into account, as the MB results confirmed for CH02. The dominance of goethite over hematite is also consistent with reflectance spectroscopy where the best-fitting routine matched goethite in seven of eight PM63 samples within the HM group, while hematite was a secondary match in four samples.

Having established that the PM63 samples have similar mixtures of goethite and hematite with similar magnetic particle-size distributions, the intensity of remanence is due to the total amount of ferric oxides in each sample. By combining the magnetization data, the total Fe concentrations from

geochemical analysis, and the MB results from CH02, an estimate of Fe apportionment in ferric oxide (hematite + goethite) can be calculated by

$$\begin{aligned} (\%Fe_{FeOx})_{sample} &= (\%Fe_{FeOx})_{CH02} \frac{(FeM)_{sample}}{(FeM)_{CH02}} \\ FeT &= \%Fe_{FeOx} + \%Fe_{mgt} + \%Fe_{sil} \end{aligned} \quad (1)$$

where $\%Fe_{FeOx}$ is the weight percentage of Fe occurring as ferric oxide in the sample, FeT is the weight percentage of total Fe in the sample, FeM is the ferric oxide remanent magnetization ($M_{Gt} + M_{Ht}$) normalized by mass at 300 K, $(\%Fe_{FeOx})_{CH02}$ is the weight percentage of total Fe in ferric oxides in CH02 and equals 1.1% as determined from MB at 4.2 K, and the percentage of Fe as ferric oxide is obtained by dividing by FeT. The Fe fraction in magnetite ($\%Fe_{mgt}$) is determined from the saturation magnetization (Fig. 5), and the remaining Fe is apportioned to paramagnetic Fe-silicate ($\%Fe_{sil}$) or structural Fe by subtraction (Table S3 in Supplementary data). The apportionment of Fe among these phases is shown Figure 11. Depending on the sample, the percentage of Fe in ferric oxides is between 40-62% (mean 51%) for the HM group. This percentage drops to 0.9-1.4% (mean 1.4%) for the three samples of the LM group. Moreover, depending on how the various minerals in HM and LM surface materials are mixed during dust events, our ferric oxide estimates can overlap with those found by Formenti et al [2014a].

4.2 Transport of iron in dust

Bristow et al. [2010] estimated a yearly Fe flux exported from the Bodélé Depression to be 1.6-6.5 Tg/yr based on geochemical analysis of dust samples collected northeast and slightly upwind from most of our surface sample locations. To convert our analysis of the ferric oxides abundances in the PM63 fraction from surface samples at dust source areas (Table S3 in Supplementary data) to yearly flux rates we make the following assumption, keeping in mind the limited number of samples analyzed. The HM group are mostly dune samples and thus are a mixture of locally derived diatomite as well as material from the underlying and surrounding sediments, whereas the LM group are almost all *in situ* diatomite sediment samples with the exception of CH26. Let the HM data be representative of the reddish (lithogenic) dust generated mostly at the margins of the diatomite-dominated central Bodélé, and the LM data be representative of diatomite-derived dust. Assuming that modern dust from central Bodélé is equal parts lithogenic + diatomite dust, the ferric oxide amount is given by the average of the HM + LM mean values given in Table S3 in Supplementary data. Under this scenario, the total Fe export as ferric oxides in dust is 0.4-1.7 Tg/yr (mean 0.9 Tg/yr), of which 69% or 0.3-1.2 Tg/yr (mean 0.6 Tg/yr) are ferric oxide nanoparticles (< 100 nm). An additional 0.008-0.034 Tg/yr (mean 0.017 Tg/yr) of Fe is exported as magnetite.

Sample CH39 was excluded from our Fe-flux calculations because it has a different provenance and a different suite of detrital minerals than our other samples, likely negating our basic assumption of similar mixtures of goethite and hematite with similar particle-size distributions. Based on the Mössbauer spectra, there is about twice as much hematite (1.9 wt%), similar amounts of goethite (1.2 wt%), and a lower fraction of FeOx occurring as nanoparticles (~50%) compared to CH02. The sample is a silty

sand collected from Angamma Delta on the northern margin of the basin fed by a river that flowed into the lake from the north with a varied catchment that includes volcanic rocks. As we have shown, CH39 is anomalous in terms of its magnetic properties, primarily due to a magnetite content (~0.5 wt%) that is 10-100 time larger than the HM and LM suite of samples. Yet the Angamma Delta sediments are surely part of the source package as they very likely get incorporated into the lithogenic component of dust and would be a potent source for fine particles of magnetite.

4.3 Implications for radiative properties and Fe bioavailability of dust plumes from the Bodélé Depression

Our results extend earlier research on the occurrences of iron-bearing minerals in Bodélé surface sediments and elsewhere in North Africa that aimed to establish linkages between dust mineralogy and potential environmental effects of dust (Lafon et al., 2004, 2006; Alfaro et al., 2004; Moreno et al., 2006; Mounkaila, 2006; Journet et al., 2008, 2104; Chudnovsky et al., 2009; Lázaro et al., 2011; Maher, 2011; Shi et al., 2011; Moosmüller et al., 2012; Adetunji, 2014; Formenti et al. 2014 a, b). These studies employed many methods for dust and soil mineralogy, including magnetic analyses, X-ray absorption analysis, X-ray diffraction, microscopy, elemental and isotopic chemistry combined with leaching experiments, as well spectroscopic techniques in the laboratory and applied to satellite retrievals. Altogether, results of these studies and ours expose remaining questions about the absolute and relative influences of different types of Fe-bearing minerals on dust radiative properties. Such influences expectedly depend on factors of substrate, weathering, origins and particle-size distributions of source sediment, as well as sorting and atmospheric processing that vary across the sub-continent and beyond. Nevertheless, our findings indicate the need to understand how high-surface-area ferric oxide nanoparticles might influence dust radiative properties.

Iron-bearing minerals supplied by aerosols are considered a significant source of bioavailable Fe to marine and terrestrial ecosystems with implications for the global carbon cycle and climate change (e.g., Jickells et al., 2005; Mahowald et al., 2009; Gassó et al., 2010). Bristow et al. (2010) estimated that 56% of the annual budget of African dust transported to the equatorial Atlantic originates from the Bodélé Depression accounting for 30 to 83% of the total Fe exported to the Atlantic Ocean. It is certain, however, that not all of this Fe is labile and bioavailable as a nutrient source in the ocean. The soluble iron fraction in mineral aerosols can vary enormously from 0.01 to 80% (Mahowald et al, 2005). Ferric oxides tend to have lower solubilities than clay minerals (Journet et al., 2008; Cwiertny et al., 2008) although the types and solubility of iron-bearing minerals carried in atmospheric dust, and the possible chemical alterations to these phases during atmospheric transport or in ocean surface waters, remain poorly understood (Shi et al., 2009, 2012; Nickovic et al., 2013).

Our results indicate that a significant fraction of the Fe oxides in the Bodélé surface sediments already occur as superparamagnetic nanoparticles (goethite, hematite, and magnetite) where they are commonly found within and on clay minerals. Relevant to our findings, experimental studies have shown that nanoparticles of ferric oxides (< 100 nm) are more chemically reactive than their crystalline

counterparts, thereby directly affecting their solubility and iron speciation during atmospheric transport and subsequent bioavailability after oceanic deposition (Cwiertny et al., 2009; Shi et al., 2009, 2012; Zhang et al., 2011; Nickovic et al., 2013). In particular, nanogoethite is predicted to have enhanced photochemical reactivity (Cwiertny et al., 2009; Zhang et al., 2011). Improved comprehension of the concentrations, mineral types, and particle-size distribution of Fe oxides at sources, as we address here, can improve understanding of the environmental effects of Fe oxides in far-traveled dust, as research continues to investigate the processes and products of atmospheric processing.

5.0 Summary and Conclusions

Our measurements of dust-source samples from the Bodélé Depression document the abundance and relative amounts of goethite, hematite, magnetite, and ferric and ferrous iron silicates. The combination of methods described herein document (1) the dominance of goethite over hematite in the examined source sediments, (2) the abundance and occurrences of their nanosize components, and (3) the ubiquity of magnetite, albeit in small amounts. Considering the intensity of recent research on the occurrences of hematite and goethite in dust and dust-source sediments, it is important to note that identifications of these minerals depend on their concentrations and variable sensitivities of different methods (e.g., Scheuven et al., 2013), such that apparent inconsistencies arise with respect to determining their absolute and relative amounts. For example, our results differ importantly from recent magnetic and diffuse reflectance spectroscopic investigations by Oldfield et al. (2014) of many of the same samples that indicated the presence of hematite only in a few of the samples. Overall, there is still much to learn about particle sizes and occurrences of Fe oxide minerals in dust, their reactivity and reactions during and after transport, and thus their effects.

Dominant goethite and subordinate hematite together compose about 2 percent of yellow-reddish dust-source sediments from the Bodélé Depression and contribute strongly to diminution of reflectance in bulk samples. These observations imply that dust plumes from the Bodélé Depression that are derived from goethite-dominated sediments strongly absorb solar radiation. A large proportion of the ferric oxide minerals, about 70 percent, occurs as nanosize particles that are commonly associated with clay minerals. As observed in SEM, many of these nanoparticles were at the surfaces of clay minerals. For all examined samples, the different mineralogic residences for total iron as averages were estimated at about 33 percent in ferric oxide minerals, 1.4 percent in magnetite, and 65 percent in ferric silicates. Structural iron in clay minerals may account for much of the iron in the ferric silicates.

The presence of ubiquitous magnetite is noteworthy for its potentially higher solubility relative to ferric oxide and for its small sizes in the BD samples, including nanosize (superparamagnetic components) and $PM < 0.1 \mu m$ (single domain). Magnetic measurements indicate similar magnetic particle-size distributions for magnetite for all samples regardless of magnetite concentration.

Finally, we estimated that the mean annual export of ferric oxides from the Bodélé Depression is 0.9 Tg/yr with 69% or 0.6 Tg/yr exported as ferric oxide nanoparticles ($< 100 \text{ nm}$). The high surface-to-

volume ratios of magnetic ferric oxide nanoparticles once entrained into dust plumes may facilitate increased atmospheric chemical and physical processing during long-distant transport and affect iron solubility and bioavailability to marine and terrestrial ecosystems.

Acknowledgments

This study was partly funded by the Climate and Land Use Change Program of the U.S. Geological Survey. The Royal Geographical Society and the Gilchrist educational trust provided funding for fieldwork (C. S. Bristow). We thank Peter Solheid, Michael Jackson, and Kimberly Yauk for helpful discussions, and with magnetic and Mössbauer spectroscopy measurements, Jiang Xiao for sample preparation and USGS magnetic and reflectance spectroscopy measurements, and George Breit for SEM analysis and interpretation and for insightful discussions regarding the mineralogy and occurrences of iron oxides. This is contribution 1509 of the Institute for Rock Magnetism, which is supported by grants from the Instruments and Facilities Program, Division of Earth Science, National Science Foundation. Any use of trade, firm, or product names is for descriptive purposes only and does not imply endorsement by the U.S. Government.

References

- Abrajevitch, A., Van der Voo, R., Rea, D.K., 2009. Variations in relative abundances of goethite and hematite in Bengal Fan sediments: Climatic vs. diagenetic signals, *Marine Geology* 267, 191–206
- Adetunji, J., 2014. ^{57}Fe Mössbauer spectroscopy investigations of iron oxidation states in the Harmattan dust nutrient contribution to West African soils. *Atmospheric Environment*, 98, 5910598.
- Alfaro, S.C., Lafon, S., Rajot, J.L., Formenti, P., Gaudichet, A., Maille, M., 2004. Iron oxides and light absorption by pure desert dust: An experimental study. *Journal of Geophysical Research* 109 D08208, doi:10.1029/2003JD004374.
- Baddock, M., Boskovic, L., Strong, C., McTainsh, G., Bullard, J., Agranovski, I., Cropp, R., 2013. Iron-rich nanoparticles formed by aeolian abrasion of desert dune sand. *Geochemistry, Geophysics, Geosystems*, 14 (9) doi: 10.1002/ggge.20229.
- Brand, R.A., 1987. Improving the validity of hyperfine field distributions from metallic alloys. Part I: Unpolarized source. *Nuclear Instruments and Methods in Physics Research B*, v. 28, p. 398-405.
- Briggs, P.H., and Meier, A.L., 2002. The determination of forty-two elements in geological materials by inductively coupled plasma–mass spectrometry, chap. I, Taggart, J.E., ed., *Analytical methods for chemical analysis of geologic and other materials*: U.S. Geological Survey Open-File Report 02–223, 16 p.
- Bristow, C.S., Hudson-Edwards, K.A., Chappell, A., 2010. Fertilizing the Amazon and equatorial Atlantic with West African dust. *Geophys. Res. Lett.* 37, L14807.
- Bristow, C.S., Drake, N., and Armitage, S., 2009. Deflation in the dustiest place on Earth: The Bodélé Depression, Chad. *Geomorphology* 105, 50-58.

- Carter-Stiglitz, B., Banerjee, S.K., Gourlan, A., Oches, E., 2006. A multi-proxy study of Argentina loess: Marine oxygen isotope stage 4 and 5 environmental record from pedogenichematite, *Palaeogeogr. Palaeoclimatol. Palaeoecol.*, 239, 45–62, doi:10.1016/j.palaeo.2006.01.008.
- Chudnovsky, A., Ben-Dor, E., Kostinski, A.B., Koren, I., 2009. Mineral content analysis of atmospheric dust using hyperspectral information from space, *Geophys. Res. Lett.*, 36, L15811, doi:10.1029/2009GL037922.
- Clark, R.N., Swayze, G.A., Wise, R., Livo, K.E., Hoeffen, T., Kokaly, R., Sutley, S.J., 2007. USGS digital spectral library splib06a, USGS Digital Data Series 231, <http://speclab.cr.usgs.gov/spectral.lib06/>.
- Cwiertny, D. M., R. M. Handler, M. V. Schaefer, V. H. Grassian, and M. M. Scherer, 2008. Interpreting nanoscale size-effects in aggregated Fe-oxide suspensions: Reaction of Fe(II) with Goethite, *Geochim. Cosmochim. Acta*, 72, 1365–1380, doi:10.1016/j.gca.2007.12.018.
- Cwiertny, D. M., Hunter, G. J., Pettibone, J. M., Scherer, M. M., and Grassian, V. H., 2009. Surface chemistry and dissolution of α -FeOOH nanorods and microrods: environmental implications of size-dependent interactions with oxalate, *J. Phys. Chem.*, 113, 2175–2186.
- Day, R., Fuller, M., Schmidt, V.A., 1977. Hysteresis properties of titanomagnetites: grain-size and compositional dependence. *Physics of the Earth and Planetary Interiors*, 13, 260–266.
- Dunlop, D. J., 2002a. Theory and application of the Day plot (Mrs/Ms v. Hcr/Hc). 1. Theoretical curves and tests using titanomagnetite data. *Journal of Geophysical Research*, 107, doi:10.1029/2001JB000487.
- Dunlop, D. J., 2002b. Theory and application of the Day plot (Mrs/Ms v. Hcr/Hc). 2. Application to data for rocks, sediments, and soils. *Journal of Geophysical Research*, 107, 1. doi:10.1029/2001JB000486.
- Dunlop, D.J., and Özdemir, Ö., 1997. *Rock Magnetism: Fundamentals and Frontiers*, 573 pp., Cambridge University Press, New York, London and Cambridge.
- Dyar, M. D., D. G. Agresti, M. W. Schaefer, C. A. Grant, E. C. Sklute, 2006. Mössbauer spectroscopy of Earth and planetary materials, *Annu. Rev. Earth Planet. Sci.*, 34, 83–125.
- Evans, M.E. and Heller, F., 2003. *Environmental Magnetism: Principles and Applications of Enviromagnetism*, London: Academic Press.
- Fabian, K., 2003. Some additional parameter to estimate domain state from isothermal magnetization measurements, *Earth and Planetary Science Letters*, 214, p. 337-345.
- Formenti, P., Caquineau, S., Chevaillier, S., Klaver, A., Desboeufs, K., Rajot, J.L., Belin, S., Briois, V., 2014a. Dominance of goethite over hematite in iron oxides of mineral dust from Western Africa: Quantitative partitioning by X-ray absorption spectroscopy. *Journal of Geophysical Research: Atmospheres*, 119, 12740-12754. 10.1002/2014JD021668.
- Formenti, P., Caquineau, S., Desboeufs, K., Klaver, A., Chevaillier, S., Journet, E., Rajot, J.L., 2014b. Mapping the physico-chemical properties of mineral dust in western Africa: Mineralogical composition, *Atmos. Chem. Phys. Discuss.*, 14, 10,241–10,310, doi:10.5194/acpd-14-10241-2014.
- Gassó, S., Grassian, V.H., Miller, R.L., 2010. Dust, climate, and ocean ecosystems. *Elements*, 6, 247–252.
- Giles, J., 2005. The dustiest place on Earth. *Nature* 434, 816-819.
- Goudie, A.S. and Middleton, N.J., 2006. *Desert dust in the global system*: Berlin, Springer, 287 p.

- Guyodo, Y. LaPara, T.M., Anschutz, A.J., Penn, R.L, Banerjee, S.K., Geiss, C.E., Zanner, W., 2006. Rock magnetic, chemical and bacterial community analysis of a modern soil from Nebraska: Earth and Planetary Science Letters 251:1-2, 168-178.
- Guyodo, Y., Mostrom, A., Penn, R.L., Banerjee, S.K., 2003. From Nanodots to Nanorods: Oriented Aggregation and Magnetic Evolution of Nanocrystalline Goethite, Geophysical Research Letters, 30 (10), doi:10.1029/2003GL017021.
- Heslop, D., and Roberts, A .P., 2012. Estimating best fit binary mixing lines in the Day plot, J. Geophys. Res., 117, B01101, doi:10.1029/2011JB008787.
- Hudson-Edwards, K. A., Bristow, C. S., Cibin, G., Mason, G., Peacock, C.L, 2014. Solid-phase phosphorus speciation in Saharan Bodélé Depression dusts and source sediments, Chemical Geology 384, 16–26
- IPCC, 2007. Climate Change 2007: Synthesis Report. Core Writing Team, Cambridge University Press, Cambridge
- Jackson, M., Solheid, P., 2010. On the quantitative analysis and evaluation of magnetic hysteresis data, Geochemistry Geophysics Geosystems 11, Q04Z15, doi:10.1029/2009GC002932.
- Jickells, T. D., An, Z. S., Andersen, K. K., Baker, A. R., Bergametti, G., Brooks, N., Cao, J. J., Boyd, P. W., Duce, R. A., Hunter, K. A., Kawahata, H., Kubilay, N., laRoche, J., Liss, P. S., Mahowald, N., Prospero, J. M., Ridgwell, A. J., Tegen, I., Torres, R., 2005. Global iron connections between desert dust, ocean biogeochemistry, and climate, Science, 308, 67–71, doi:10.1126/science.1105959.
- Jeong, G.Y., Nousiainen, T., 2014. TEM analysis of the internal structures and mineralogy of Asian dust particles and the implications for optical modeling. Atmospheric Chemistry and Physics Discussions, 14, 6619-6661, doi:10.5194/acpd-14-6619-2014.
- Jiang, Z., Q. Liu, Q., Dekkers, M. J., Colombo, C., Yu, Y., Barron, V. Torrent, J., 2014. Ferro and antiferromagnetism of ultrafinegrained hematite, Geochem. Geophys. Geosyst., 15, 2699–2712, doi:10.1002/2014GC005377.
- Journet, E., Desboeufs, K. V., Caquineau, S., Colin, J.-L., 2008. Mineralogy as a critical factor of dust iron solubility, Geophys. Res. Lett., 35, L07805, doi:10.1029/2007GL031589.
- Journet, E., Balkanski, Y., Harrison, S.P., 2014. A new data set of soil mineralogy for dust-cycle modeling. Atmos. Chem. Phys., 14, 3801–3816, doi:10.5194/acp-14-3801-2014.
- King, J.W., Channel, J.E.T., 1991. Sedimentary magnetism, environmental magnetism, and magnetostratigraphy. Reviews of Geophysics, Supplement, 358–370.
- Kokaly, R.F., 2011. PRISM: Processing routines in IDL for spectroscopic measurements (installation manual and user's guide, version 1.0). U.S. Geological Survey Open-File Report 2011–1155, 431 p. <http://pubs.usgs.gov/of/2011/1155/>.
- Kokaly, R. F., and Skidmore, A. K. , 2015. Plant phenolics and absorption features in vegetation reflectance spectra near 1.66 μm . International Journal of Applied Earth Observation and Geoinformation. Available online February 7, 2015. doi:10.1016/j.jag.2015.01.010
- Koren, I. and Kaufman, Y.J., 2004. Direct wind measurements for Saharan dust events from Terra and Aqua satellites. Geophysical Research Letters, 31 (6) L06122.
- Kusnir, Imrich, 1995. Géologie, Ressources Minérales, et Ressources en Eau du Tchad. Travaux et Documents Scientifiques du Tchad, Série Connaissance du Tchad, no. 1, 115 pp.
- Lafon, S., Rajot, J-L., Alfaro, S.C., Gaudichet, A., 2004. Quantification of iron oxides in desert aerosol. Atmospheric Environment 38 1211-1218. doi:10.1016/j.atmosenv.2003.11.006.

- Lafon, S., Sokolik, I.N., Rajot, J. L., Caquineau, S., A. Gaudichet, 2006. Characterization of iron oxides in mineral dust aerosols: Implications for light absorption, *Journal of Geophysical Research* 111 D21207, doi:10.1029/2005JD007016.
- Lázaro, F.J., Gutiérrez, L., Barrón, V., Gelado, M.D., 2011. The speciation of iron in desert dust collected in Gran Canaria (Canary Islands): Combined chemical, magnetic and optical analysis *Atmospheric Environment* 42, 8987-8996, doi:10.1016/j.atmosenv.2008.09.035.
- Liu, Qingsong, Yu, Yongjia, Torrent, José, Roberts, A.P., Pan, Yongxin, Zhu, Rixiang, 2006. Characteristic low-temperature magnetic properties of aluminous goethite [α -(Fe, Al)OOH] explained, *Journal of Geophysical Research*, v. 111, B12S34, 12 p.
- Maher, B. A., Karloukovski, V.V, Mutch, T. J., 2004. High-field remanence properties of synthetic and natural submicrometre hematites and goethites: Significance for environmental contexts, *Earth Planet. Sci. Lett.*, 226, 491–505, doi:10.1016/j.epsl.2004.05.042.
- Maher, B.A., 2011. The magnetic properties of Quaternary aeolian dusts and sediments, and their paleoclimatic significance. *Aeolian Research* 3, 87-144, doi:10.1016/j.aeolia.2011.01.005.
- Mahowald, N.M., Engelstaedter, Sebastian, Luo, Chao, Sealy, Andrea, Artaxo, Paulo, Benitez-Nelson, Claudia, Bonnet, Sophie, Chen, Ying, Chuang, Patrick Y., Cohen, David D., Dulac, Francois, Herut, Barak, Johansen, Anne M., Kubilay, Nilgun, Losno, Remi, Maenhaut, Willy, Paytan, Adina, Prospero, Joseph M., Shank, Lindsay M., Siefert, Ronald L, 2009. Atmospheric iron deposition: global distribution, variability, and human perturbations. *Annu. Rev. Mar. Sci.* 1, 245–278.
- Mahowald, N. M., A. R. Baker, G. Bergametti, N. Brooks, R. A. Duce, T. D. Jickells, N. Kubilay, J. M. Prospero, I. Tegen, 2005. Atmospheric global dust cycle and iron inputs to the ocean, *Global Biogeochem. Cycles*, 19, GB4025, doi:10.1029/2004GB002402.
- Moosmüller, H., Engelbrecht, J. P., Skiba, M., Frey, G., Chakrabarty, R. K., and Arnott, W. P., 2012. Single scattering albedo of fine mineral dust aerosols controlled by iron concentration, *Journal of Geophysical Research*, 117, D11210, doi:10.1029/2011JD016909, 10.1029/2011JD016909
- Moreno, T. Querol, X., Castillo, S., Alastuey, A., Cuevas, E., Herrmann, L., Mounkila, M., Elvira, J., Gibbons, W., 2006. Geochemical variations in aeolian mineral particles from the Sahara-Sahel dust corridor. *Chemosphere* 65, 261-270.
- Morris, R.V., Schulze, D.G., Lauer Jr., H.V., Agresti, D.G., Shelfer, T.D., 1992. Reflectivity (visible and near IR), Mössbauer, static magnetic, and X ray diffraction properties of aluminum-substituted hematites. *Journal of Geophysical Research* 97(E6), 10257–10266, doi:10.1029/92JE00455.
- Mounkaila, M., 2006. Spectral and mineralogical properties of potential dust sources on a transect from the Bodélé Depression (central Sahara) to the Lake Chad in the Sahel. *Hohenheimer Bodenkunliche Hefte*, 78, 1-11.
- Nickovic, S., Vukovic, A., Vujadinovic, M., 2013. Atmospheric processing of iron carried by mineral dust. *Atmos. Chem. Phys.* 13, 9169–9181
- Oldfield F., R.C. Chiverrell, R. Lyons, E. Williams, Z. Shen, C. Bristow, J. Bloemendal, J. Torrent, J.F. Boyle, 2014. Discriminating dusts and dusts sources using magnetic properties and hematite:Goethite ratios of surface materials and dust from North Africa, the Atlantic and Barbados, *Aeolian Research* 13, 91–104
- Özdemir, Ö., and Dunlop, D. J., 2010. Hallmarks of maghemitization in low-temperature remanence cycling of partially oxidized magnetite nanoparticles, *J. Geophys. Res.*, 115, B02101, doi:10.1029/2009JB006756.

- Özdemir, Ö., and Dunlop, D. J., 2014. Hysteresis and coercivity of hematite, *J. Geophys. Res. Solid Earth*, 119, doi:10.1002/2013JB010739.
- Özdemir, Ö., Dunlop, D. J., Berquó, T.S., 2008. Morin Transition in Hematite: Size Dependence and Thermal Hysteresis, *Geochem. Geophys. Geosys.*, 9, Q10Z01, doi:10.1029/2008GC002110.
- Prospero JM, Ginoux P, Torres O, Nicholson SE, Gill TE., 2002. Environmental characterization of global sources of atmospheric soil dust identified with the NIMBUS 7 Total Ozone Mapping Spectrometer (TOMS) absorbing aerosol product. *Reviews of Geophysics* 40: 1002, DOI:10.1029/2001JD000963.
- Reynolds, R.L, Cattle, S.R., Moskowitz, B.M., Goldstein, H.L., Yauk, K., Flagg, .C.B., Berquó, T.S. , Kokaly, R.F. , Morman, S., Breit, G.N., 2014a. Iron oxide minerals in dust of the Red Dawn event in eastern Australia, September 2009, *Aeolian Research*, *Aeolian Research* 15, 1–13.
- Reynolds, R. L., Goldstein, H.L., Moskowitz, B.M., Bryant, A.C., Skiles, S.M., Kokaly, R.F., Flagg, C.B., Yauk, K., Berquó, T.S. Breit, G.N., Ketterer, M., Fernandez, D., Miller, M.E., Painter, T.H., 2014b. Composition of dust deposited to snow cover in the Wasatch Range (Utah, USA): Controls on radiative properties of snow cover and comparison to some dust-source sediments, *Aeolian Research*, 15, 73–90.
- Roberts, A. P., Cui, Y.-L., Verosub, K. L. 1995. Waspwaisted hysteresis loops: mineral magnetic characteristics and discrimination of components in mixed magnetic systems. *Journal of Geophysical Research B: Solid Earth*, 100, 17909–17924
- Rochette, P., Fillion, G., 1989. Field and temperature behavior of remanence in synthetic goethite: Paleomagnetic implications, *Geophys. Res. Lett.*, 16, 851–854.
- Rochette, P., Mathe, P.E., Esteban, L., Rakoto, H., Bouchez, J.L., Liu, Q., Torrent, J., 2005. Non-saturation of the defect moment of goethite and fine-grained hematite up to 57 teslas, *Geophys. Res. Lett.*, 32, L2239, doi:10.1029/2005GL024196.
- Schaepman-Strub, G., Schaepman, M.E., Painter, T.H., Dangel, S., Martonchik, J.V., 2006. Reflectance quantities in optical remote sensing—definitions and case studies. *Remote Sens. Environ.* 103 (1), 27–42.
- Scheuven D., Schütz L., Kandler K., Ebert M., Weinbruch, 2013. Bulk composition of northern African dust and its source sediments—A compilation. *Earth-Science Reviews*, 116, 170–194.
- Shi, Z., Krom, M.D., Bonneville, S., Baker, A.R., Jickells, T.D., Benning, L.G., 2009. Formation of iron nanoparticles and increase in iron reactivity in the mineral dust during simulated cloud processing. *Environ. Sci. Technol.* 43, 6592–6596.
- Shi, Z., Krom, M.D., Bonneville, S., Baker, A.R., Bristow, C., Drake, N., Mann, G., Carslaw, K., McQuaid, J.B., Jickells, T., Benning, L.G., 2011. Influence of chemical weathering and aging of iron oxides on the potential iron solubility of Saharan dust during simulated atmospheric processing. *Global Biogeochem. Cycles* 25, GB2010. <http://dx.doi.org/10.1029/2010GB003837>.
- Shi, Z., Krom, M.D., Jickells, T.D., Bonneville, S., Carslaw, K.S., Mihalopoulos, N., Baker, A.R., Benning, L.G., 2012. Impacts on iron solubility in the mineral dust by processes in the source region and the atmosphere: A review. *Aeolian Res.* 5, 21–42.
- Smirnov, A.V., Tarduno, J.A., 2000. Low-temperature magnetic properties of pelagic sediments (Ocean Drilling Programme Site 805C): tracers of maghemitization and magnetic mineral reduction, *J. geophys. Res.*, 105, 16 457–16 471.

- Sokolik, I.N., Toon, O.B., 1999. Incorporation of the mineralogical composition into models of the radiative properties of mineral aerosol from UV to IR wavelengths. *Journal of Geophysical Research* 104 (D8), 9423–9444.
- Tauxe, L., Mullender, T. A. T. & Pick, T. 1996. Potbellies, wasp-waists, and superparamagnetism in magnetic hysteresis. *Journal of Geophysical Research B, Solid Earth*, 101, 571–583.
- van der Zee, C., Roberts, D.R., Rancourt, D.G., Slomp, C.P., 2003. Nanogoethite is the dominant reactive oxyhydroxide phase in lake and marine sediments. *Geology* 31, 993–996.
- Vandenberghe, R.E., De Grave, E., Landuydt, C., Bowen, L.H., 1990. Some aspects concerning the characterization of iron oxides and hydroxides in soils and clays. *Hyperfine Interact.* 53, 175–196.
- Vandenberghe, R.E., Van San, E., De Grave, E., DaCosta, G.M., 2001. About the Morin transition in hematite in relation with particle size and aluminum substitution. *Czech. J. Phys.* 51, 663–675.
- Warren, A., Chappell, A., Todd, M.C., Bristow, C., Drake, N., Engelstaedter, S., Martins, V., M’bainayel, S., Washington, R., 2007. Dust-raising in the dustiest place on earth: Geomorphology 9225-37, doi:10.1016/j.geomorph.2007.02.007.
- Washington, R. and Todd, M.C., 2005. Atmospheric controls on mineral dust emission from the Bodélé Depression, Chad. *Geophysical Research Letters*, 32 (17), L17701.
- Washington R, Todd MC, Lizcano G, Tegen I, Flamant C, Koren I, Ginoux P, Engelstaeder S, Bristow CS, Zender CS, Goudie AS, Warren A, Prospero JM. 2006. Links between topography, wind, deflation, lakes, and dust: The case of the Bodélé Depression, Chad. *Geophysical Research Letters* 33, L09401. DOI:10.1929/2006GL025827.
- Washington R, Todd MC, Middleton NJ, Goudie AS. 2003. Dust-storm source areas determined by the Total Ozone Monitoring Spectrometer and surface observations. *Annals of the Association of American Geographers* 93 (2): 297-313.
- Wolf, R.E., and Adams, Monique, 2015. Multi-elemental analysis of aqueous geochemical samples by quadrupole inductively coupled plasma-mass spectrometry (ICP-MS): U.S. Geological Survey Open-File Report 2015–1010, p. 34, <http://dx.doi.org/10.3133/ofr20151010>.
- Worm, H. U. 1998. On the superparamagnetic-stable single domain transition for magnetite, and frequency dependence of susceptibility. *Geophysical Journal International*, 133, 201–206.
- Yu, H., Chin, M., Yuan, T., Bian, H., Remer, L. A., Prospero, J. A., Omar, A., Winker, D., Yang, Y., Zhang, Y., Zhang, Z., Zhao, C., 2015. The fertilizing role of African dust in the Amazon rainforest: A first multiyear assessment based on data from Cloud-Aerosol Lidar and Infrared Pathfinder Satellite Observations, *Geophys. Res. Lett.*, 42, 1984–1991, doi:10.1002/2015GL063040.
- Zhang, Hengzhong, Meredith Bayne, Sandra Fernando, Benjamin Legg, Mengqiang Zhu, R. Lee Penn, Jillian F. Banfield, 2011. Size-Dependent Bandgap of Nanogoethite, *The Journal of Physical Chemistry C* 2011 115 (36), 17704-17710

Figures

Figure 1. Location of Bodélé Depression and sampling sites used in this study.

Figure 2. Reflectance spectra across solar radiation spectrum (wavelength range from 0.35 to 2.50 μm) for sample CH08. Spectra measured for three different particle size fractions: fine (PM63, solid line), medium (63-125 μm , dashed-line), and coarse (125-2000 μm , dotted-line).

Figure 3. Box plot of HIRM sorted by particle size fractions for Bodélé surface sediment. The 25th (lower edge of the box), 50th (horizontal line through the box) and the 75th (upper edge of the box) percentiles of the distributions of values are shown. Whiskers below and above the box represent the minimum and maximum value. Note the vertical axis is logarithmic.

Figure 4. Average visible reflectance plotted against HIRM for different particle size fractions. All samples for which magnetic measurements at USGS and IRM were made are included. Note the vertical axis is logarithmic

Figure 5. Magnetite concentration for Bodélé surface sediments in PM63 and coarse (63-125 μm) particle size fractions. The magnetite concentration for sample CH39 is more than an order of magnitude greater than the other samples (0.57%) and is not included.

Figure 6. Day plot of remanence ratio (M_r/M_s) against coercivity ratio (H_{cr}/H_c). Solid lines are theoretical SD + MD (single domain + multidomain) and SD + SP (single-domain + superparamagnetic) mixing curves based on linear mixing models for magnetite from Dunlop (2002). The mixing curves are admixture of end member magnetites corresponding to SD ($< 0.1\mu\text{m}$), MD (15 μm), and SP (10 nm) particle sizes. The two SD-MD curves use different SD components: oxidized (SD2) and unoxidized (SD1). Parameters derived from hysteresis loops: M_r , remanent magnetization; M_s , saturation remanent magnetization; H_c , coercivity; H_{cr} , coercivity of remanence.

Figure 7. Low temperature magnetization curves for PM63 samples after zero-field cooling. Each curve is normalized to the initial remanent magnetization at 10 K and measurements are collected in zero-field on warming to 300 K. Black lines are HM samples, gray lines are LM samples, and dashed-line is CH39. There are no indications of Verwey Transition ($T \sim 100$ K) due to magnetite nor the Morin Transition ($T \sim 250$ K) due to hematite.

Figure 8. Low-temperature magnetization thermal cycles following the Carter-Guyodo method. Initial remanence acquired in a 2.5 T field after cooling from 400 K to 300 K, and then partially demagnetized in a peak alternating field of 0.2 T. Remanence is measured on cooling from 300–20 K, warming from 20–400 K, cooling from 400–20 K, and then warming back to 300 K. M_{Gt} and M_{Ht} indicate the remanence contribution from goethite and hematite, respectively. (a) High-magnetization (HM) sample (CH02). Non-reversible loss of remanence on heating from 300 to 400 K and cooling back to 300 K indicates the presence of goethite. (b) Low-magnetization (LM) sample (CH62). Both the low and high temperature cycles are practically reversible, but the greater than 2-fold increase in remanence on cooling to 20 K indicates the presence of goethite. The Morin transition ($T \sim 250$ K) is suppressed in both samples.

Figure 9. Percentage of remanence carried by goethite (M_{Gt}) and hematite (M_{Ht}) for PM63 samples. The remaining percentage is carried by magnetite/maghemite. Remanence values determined by the Carter-Guyodo method as shown in Fig. 8a.

Figure 10. Scanning electron micrograph of particles in a laminated diatomite sample (CH82). (a) Secondary electron image. Iron oxide (~15 wt. % Fe) interpreted to be a thin coating on a smectite particle in area 1. A similar iron oxide coating (~25 wt. % Fe) with kaolinite in area 2. Clay minerals that contain structural iron (<4 wt. % Fe) reside on a Na-SO₄ particle in area 3. (b) Backscatter electron micrograph of the same area as in (a).

Figure 11. Iron speciation of PM63 Bodélé surface sediment estimated by magnetization and Mössbauer spectroscopy. Ferric oxide (FeOx) is the sum of goethite and hematite and wt% Fe is the total Fe determined by chemical analysis. See text for further details.

Table 1. Description and Locations of Bodélé Samples.

Sample #	Latitude	Longitude	Sample description
CH02	N 16° 52' 58.2"	E 18° 31' 20.5"	Dune crest
CH08	N 16° 55' 29.9"	E 18° 22' 42.6"	Dark dune diatomite flakes and sand from barchan horn
CH09	N 16° 55' 47.7"	E 18° 22' 30.7"	Diatomite from barchan horn
CH11	N 16° 55' 28.6"	E 18° 13' 51.7"	Diatomite peds
CH23	N 16° 46' 45.6"	E 18° 17' 57.5"	Basal diatomite overlying dune sand
CH24	N 16° 46' 45.6"	E 18° 17' 57.5"	Grey diatomite 30cm above dune sand
CH25	N 16° 46' 45.6"	E 18° 17' 57.5"	Top diatomite 1.25m above dune sand
CH26	N 16° 51' 10.1"	E 18° 14' 44.6"	Dune diatomite flakes and sand from megaripples on interdune
CH39	N 17° 36' 54.1"	E 17° 36' 11.2"	Fine micaceous sand with ostracodes (Angamma Delta)
CH50	N 16° 40' 35.8"	E 17° 46' 39.9"	Diatomite outcrop on top of pink sand
CH62	N 16° 41' 03.2"	E 18° 01' 42.0"	Mesa capped by 30 cm pale grey mud ¹
CH77	N 16° 53' 55.0"	E 18° 28' 03.6"	Saltating particles during dust storm 9/3/2005
CH80	N 16° 54' 35.4"	E 18° 26' 47.5"	Diatomite breccia in dune sediment
CH81	N 16° 54' 35.4"	E 18° 26' 47.5"	Coarse diatomite particles in dune deposit
CH82	N 16° 54' 35.4"	E 18° 26' 47.5"	Fine diatomite particles in laminated dune deposit

¹Probably distal sediment from delta Bahr el Ghazal.

Table 2. Summary of results from reflectance spectra and phases detected by magnetic, Mössbauer, and reflectance spectroscopy for PM63 sized fraction.

Sample	Group	Particle Size (μm)	AVR	ATR	Color	RS	MB	Magnetic
CH02	HM	<63	0.187054	0.462420	7.5 YR 6/3	Gt,Ht	Ht, nGt	Mgt, Ht, Gt, Sp
CH08	HM	<63	0.223177	0.474907	7.5 YR 6/3	Gt,Ht	*	Mgt, Ht, Gt, Sp
CH09	HM	<63	0.221818	0.485637	7.5 YR 6/3	Gt,Ht	*	*
CH11	HM	<63	0.236691	0.483308	7.5 YR 6/3	Gt,Ht	*	Mgt, Ht, Gt, Sp
CH23	LM	<63	0.330275	0.659640	10 YR 7/2	none	*	Mgt, Ht, Gt, Sp
CH24	LM	<63	0.351506	0.560176	10 YR 7/1	none	Pm	Mgt, Ht, Gt, Sp
CH25	LM	<63	0.423592	0.658529	2.5 Y 8/1	none	*	*
CH26	LM	<63	0.400538	0.630689	2.5 Y 8/2	none	*	*
CH39	none	<63	0.165966	0.337016	10 YR 7/1	Gt	Ht, nGt	Mgt, Ht, Gt, Sp
CH50	LM	<63	0.476396	0.691272	10 YR 8/1	none	*	*
CH62	LM	<63	0.341190	0.618396	5 YR 7/2	none	Pm	Mgt, Ht, Gt, Sp
CH77	LM	<63	0.208391	0.473267	7.5 YR 6/3	Gt,Ht	*	*
CH80	HM	<63	0.318649	0.524297	10 YR 7/2	none	*	Mgt, Ht, Gt, Sp
CH81	HM	<63	0.258654	0.498592	10 YR 6/2	Gt	*	Mgt, Ht, Gt, Sp
CH82	HM	<63	0.202274	0.470174	7.5 YR 6/3	Gt,Ht	*	*

Magnetite/maghemite (Mgt), hematite (Ht), goethite (Gt), nanogoethite (nGt), and paramagnetic iron silicates (Pm). Sp=superparamagnetic (nanophase) behavior detected but not possible to assign a particular magnetic phase (magnetite, hematite, or goethite). HM=high magnetization sample group; LM=low magnetization sample group. Average total reflectance (ATR) is average reflectance over entire wavelength range (0.35 to 2.50 μm) and average visible reflectance (AVR) is average reflectance over visible wavelengths (0.40 to 0.70 μm). Detection methods include: magnetic (low-temperature remanence curves), Mössbauer spectroscopy (MB) at 300 K and 4.2 K, and reflectance spectroscopy (RS). *= did not measure with Mössbauer spectroscopy or low-temperature magnetometry.

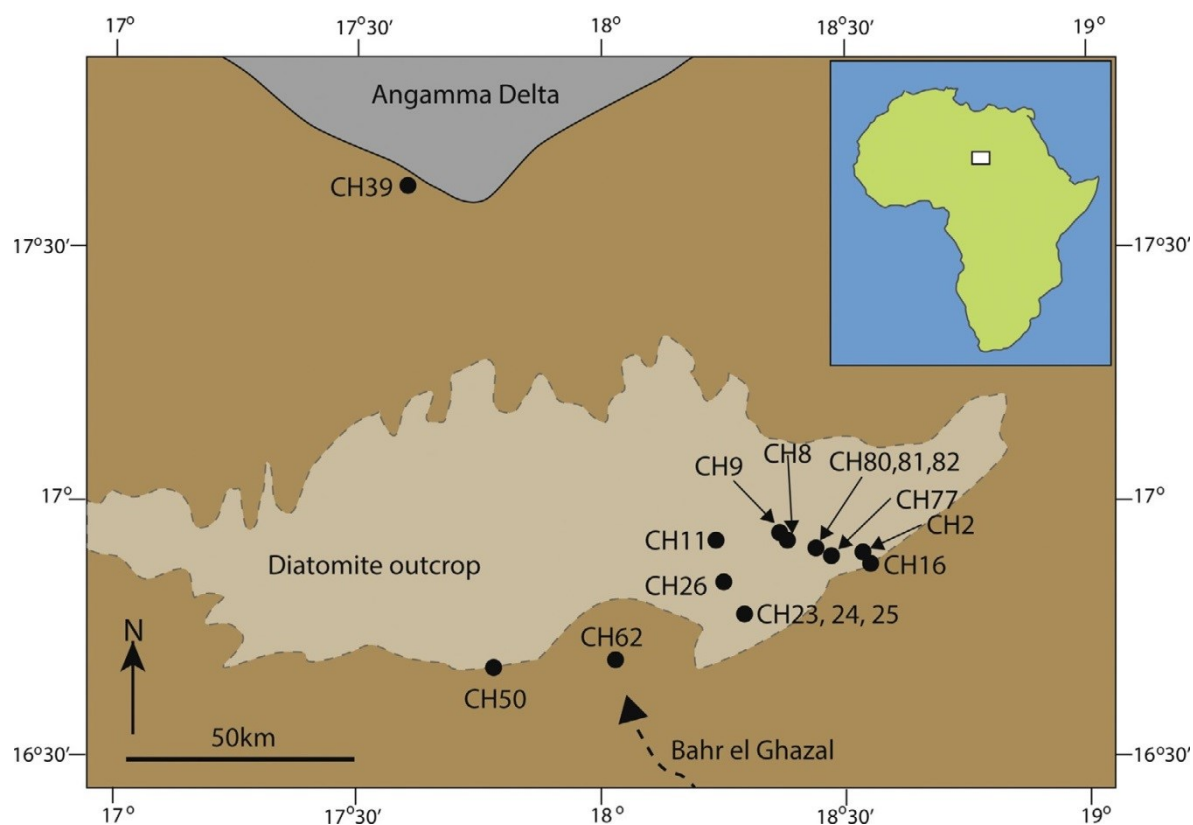


Figure 1

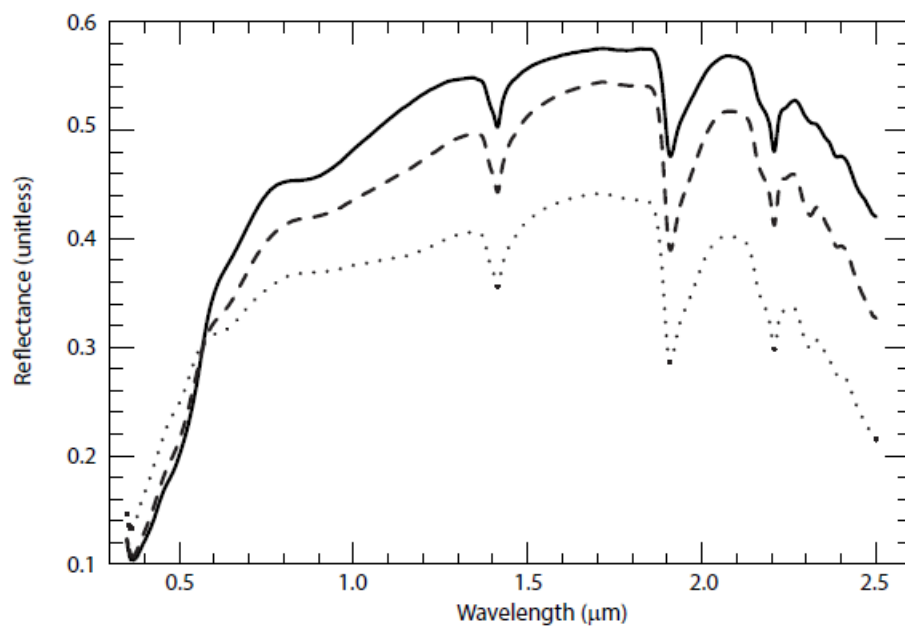


Figure 2

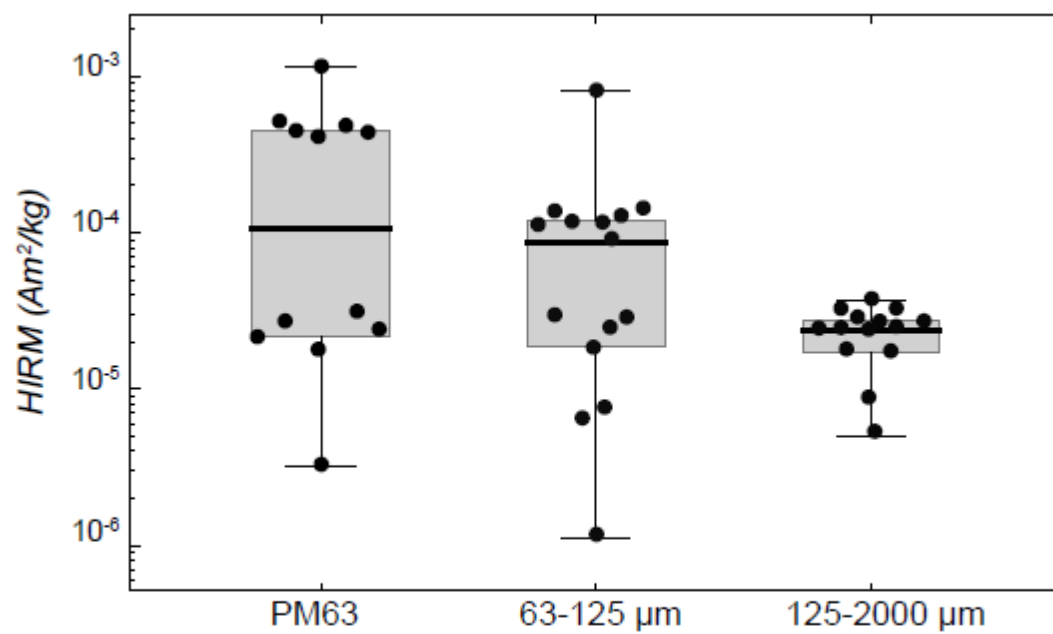


Figure 3

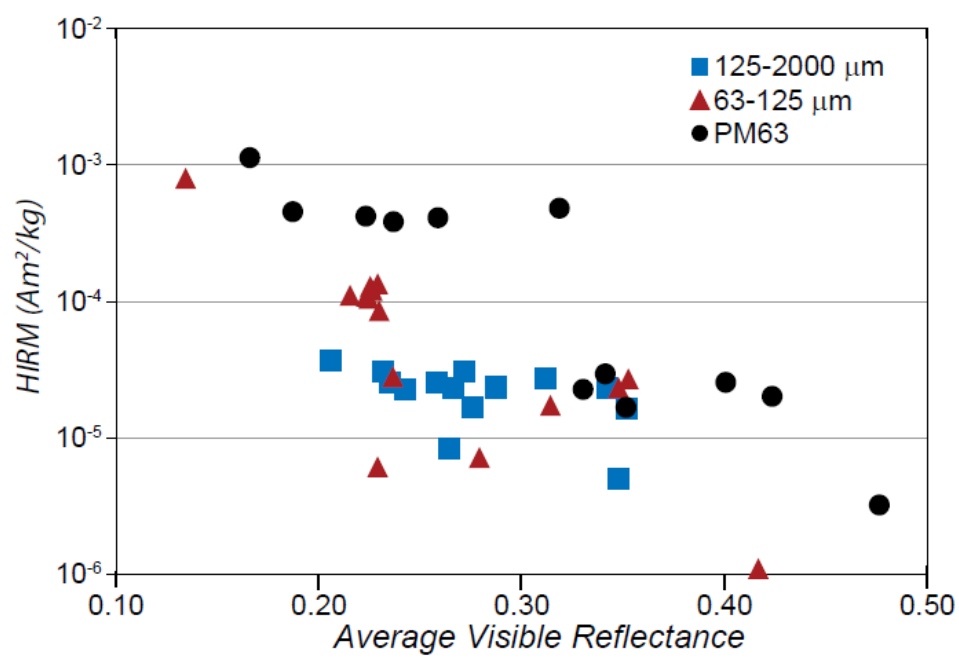


Figure 4

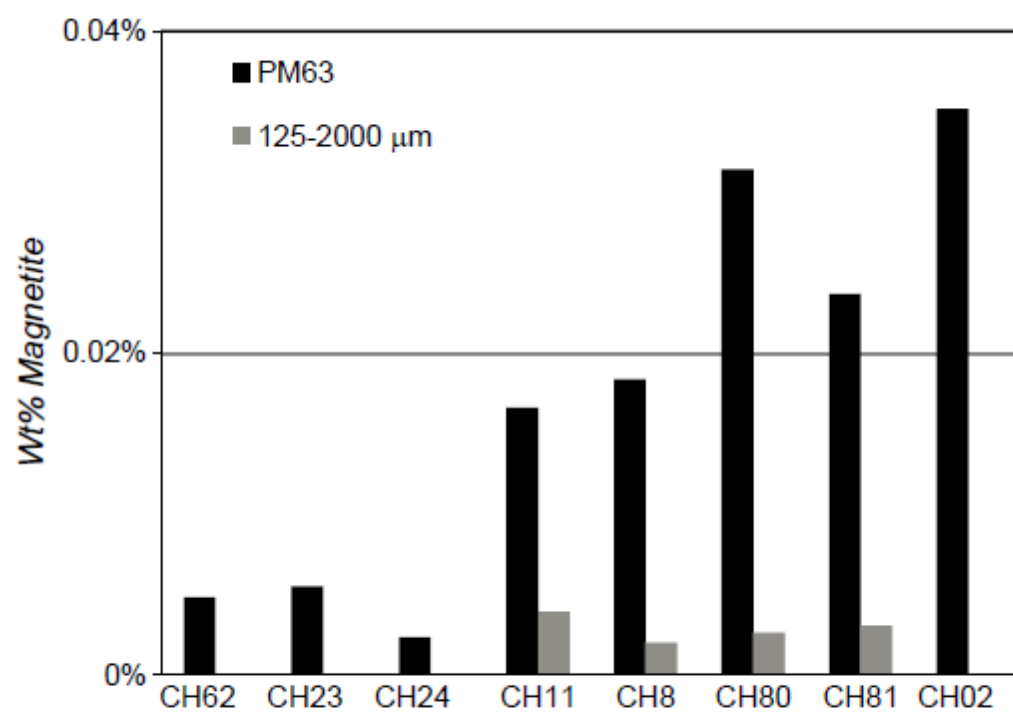


Figure 5

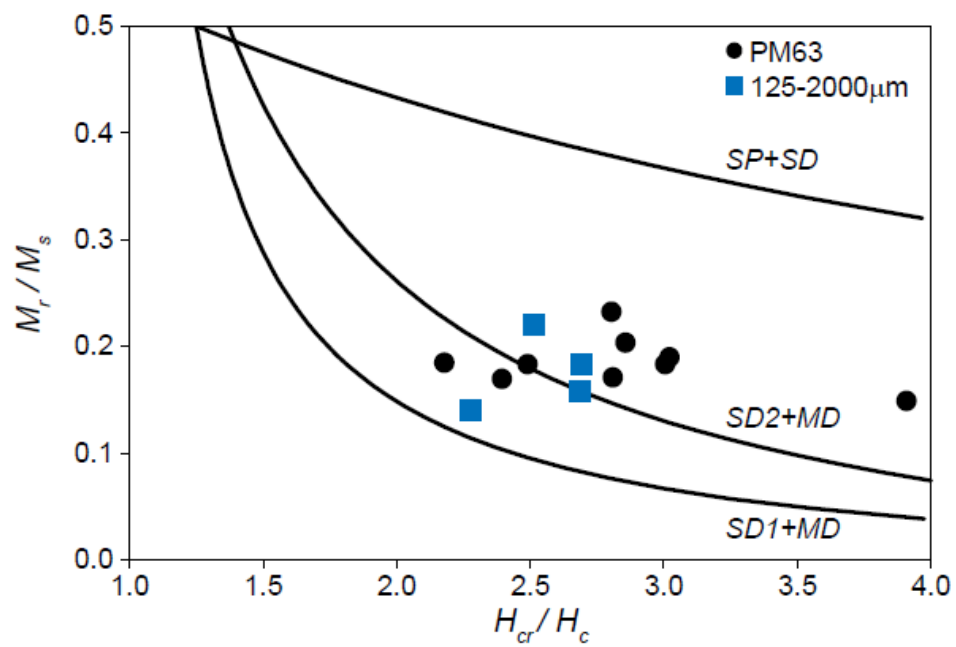


Figure 6

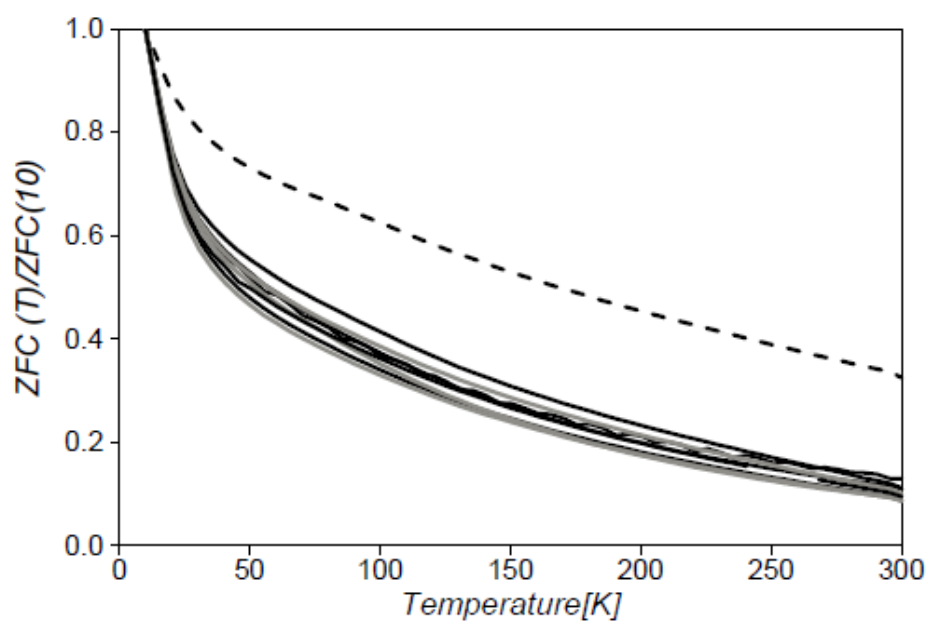


Figure 7

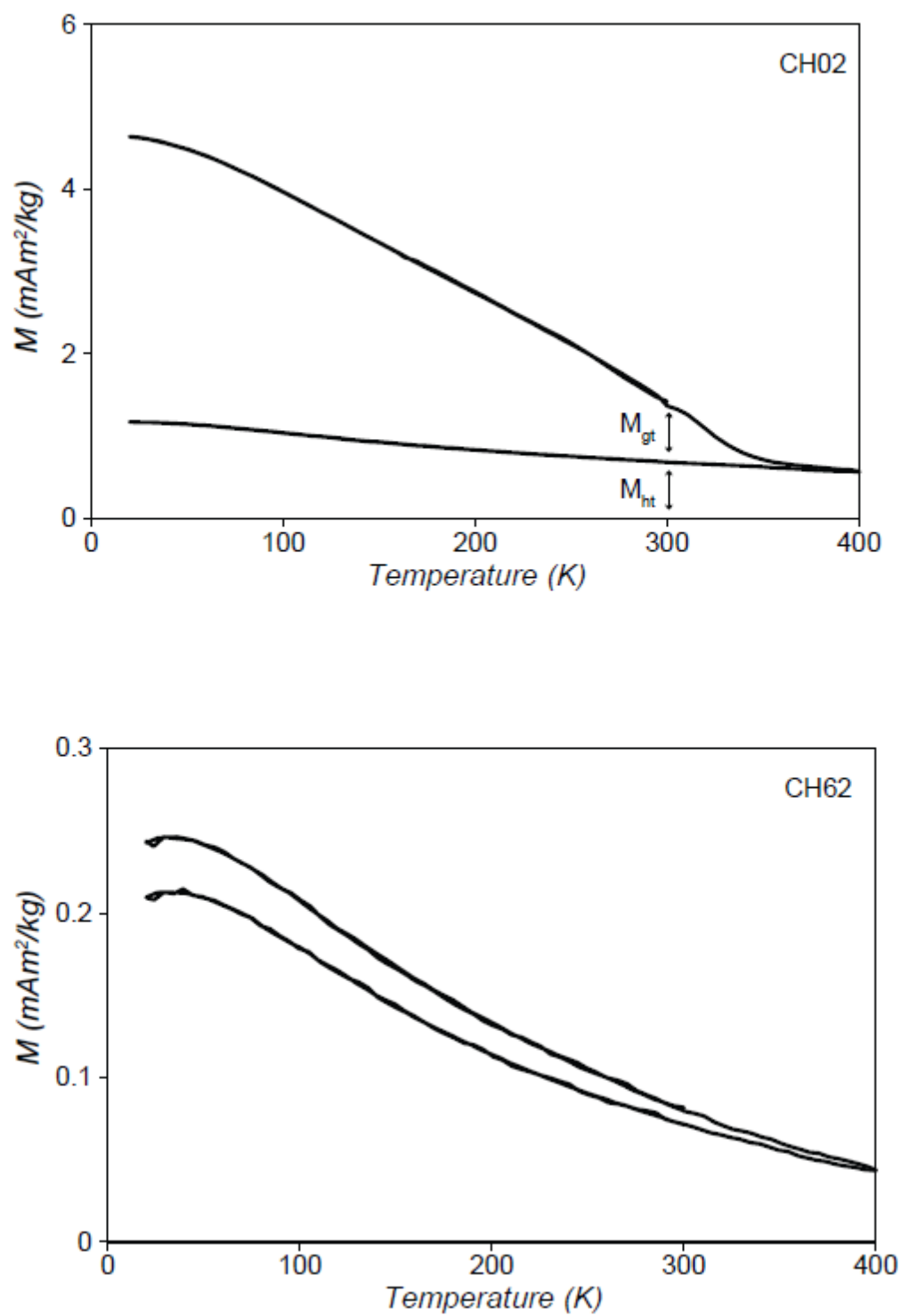


Figure 8

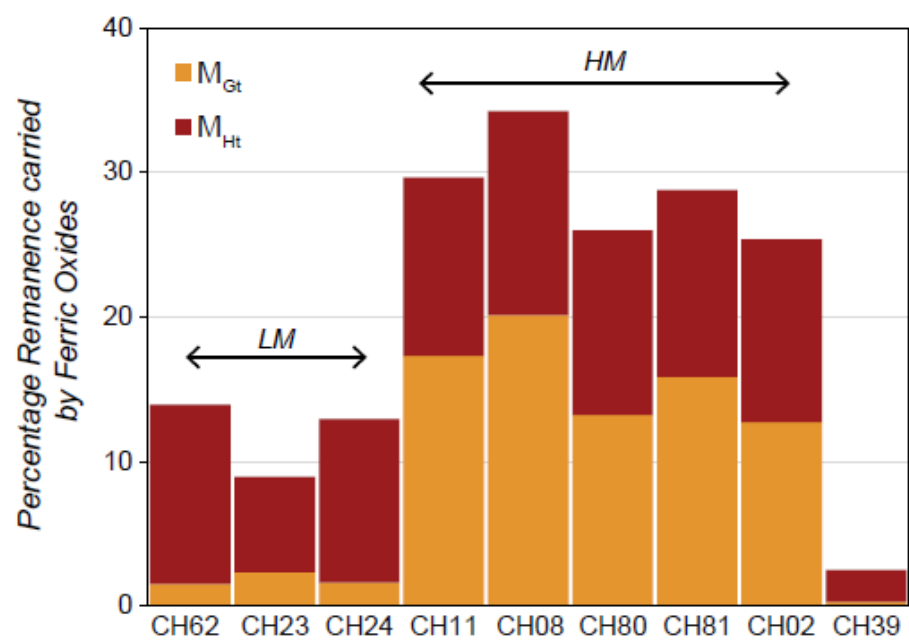
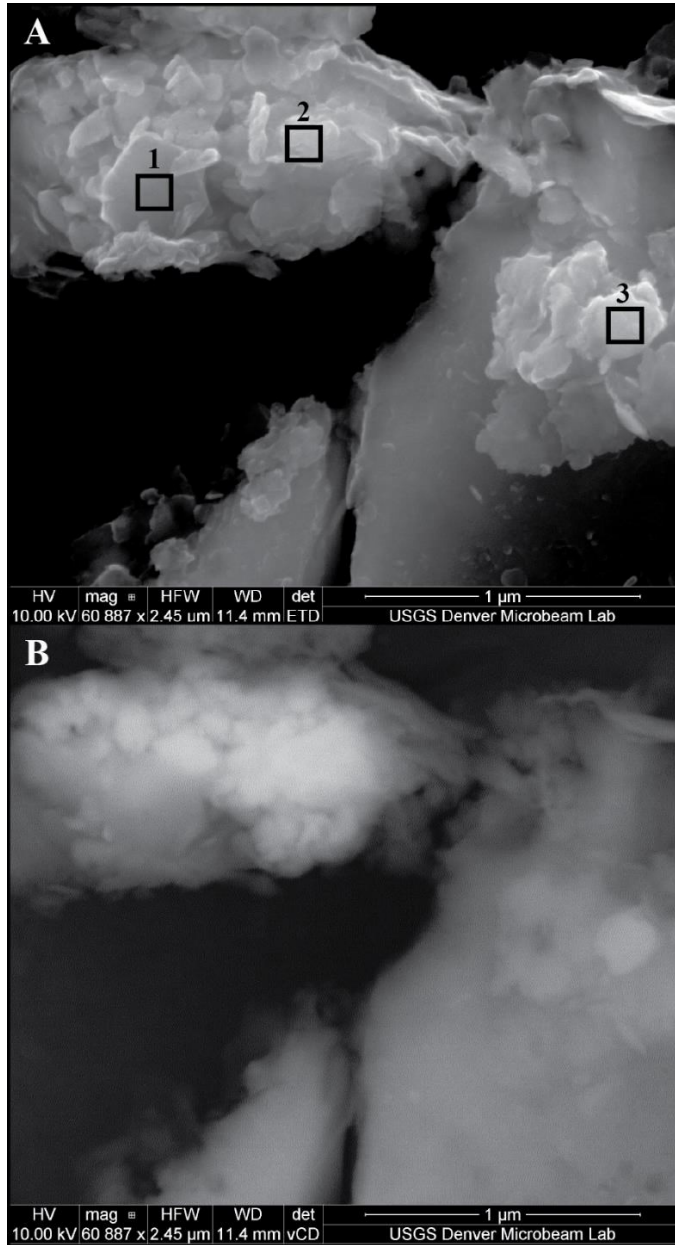


Figure 9



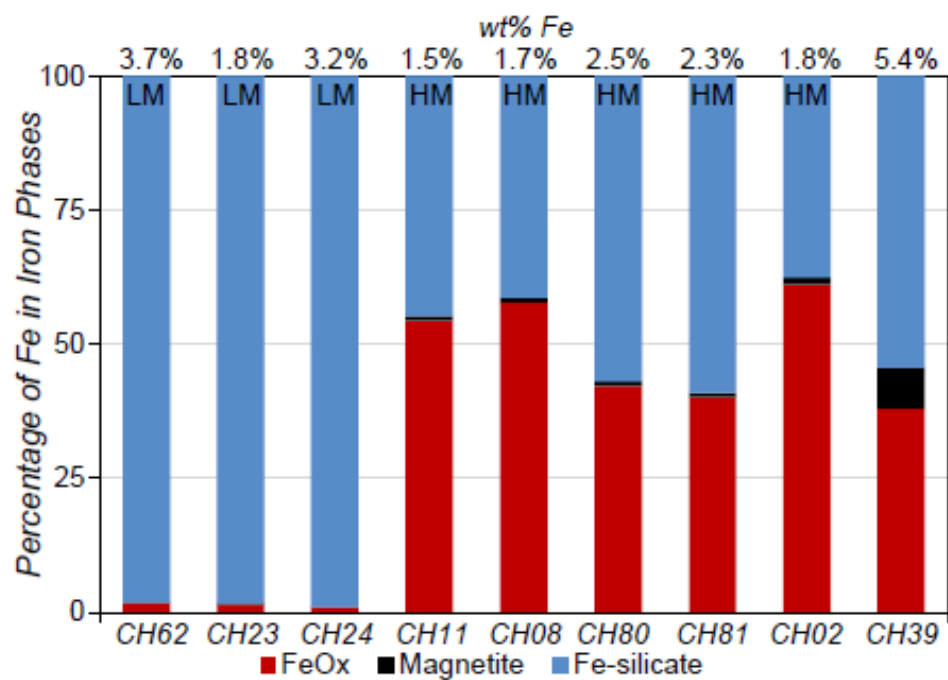


Figure 11

Supplementary Material

Iron oxide minerals in dust-source sediments from the Bodélé Depression, Chad: Implications for radiative properties and Fe bioavailability of dust plumes from the Sahara

Bruce M. Moskowitz^{1*}, Richard L. Reynolds^{1,2}, Harland L. Goldstein², Thelma Berquó³, Raymond F. Kokaly², and Charlie S. Bristow⁴

¹Institute for Rock Magnetism, Department of Earth Sciences, University of Minnesota, Minneapolis, Minnesota, USA

²U.S. Geological Survey, Denver, Colorado, USA

³Department of Physics, Concordia College, Moorhead, Minnesota, USA

⁴School of Earth Sciences, Birkbeck College, University of London, Malet St., London WC1E 7HX, UK

This supplementary material includes 4 tables and 8 figures

Table S1. Summary of results from reflectance spectra for Bodélé Surface Sediments.

Sample #	Particle Size (µm)	AVR	ATR	Color	RS
CH02	<63	0.187054	0.462420	7.5 YR 6/3	Gt,Ht
CH08	<63	0.223177	0.474907	7.5 YR 6/3	Gt,Ht
CH09	<63	0.221818	0.485637	7.5 YR 6/3	Gt,Ht
CH11	<63	0.236691	0.483308	7.5 YR 6/3	Gt,Ht
CH23	<63	0.330275	0.659640	10 YR 7/2	none
CH24	<63	0.351506	0.560176	10 YR 7/1	none
CH25	<63	0.423592	0.658529	2.5 Y 8/1	none
CH26	<63	0.400538	0.630689	2.5 Y 8/2	none
CH39	<63	0.165966	0.337016	10 YR 7/1	Gt
CH50	<63	0.476396	0.691272	10 YR 8/1	none
CH62	<63	0.341190	0.618396	5 YR 7/2	none
CH77	<63	0.208391	0.473267	7.5 YR 6/3	Gt,Ht
CH80	<63	0.318649	0.524297	10 YR 7/2	none
CH81	<63	0.258654	0.498592	10 YR 6/2	Gt
CH82	<63	0.202274	0.470174	7.5 YR 6/3	Gt,Ht
CH02	63-125	0.226373	0.488754	10 YR 6/4	Gt
CH08	63-125	0.223305	0.428892	2.5 Y 6/2	Gt
CH09	63-125	0.228987	0.408243	7 YR 7/2	none
CH11	63-125	0.225318	0.426878	10 YR 6/2	Gt
CH23	63-125	0.279026	0.612502	2.5 Y 7/2	none
CH24	63-125	0.314158	0.508398	2.5 Y 7/1	none
CH25	63-125	0.352525	0.598230	2.5 Y 8/1	none
CH26	63-125	0.347773	0.573504	2.5 Y 8/1	none
CH39	63-125	0.134215	0.260812	2.5 Y 5/2	Gt
CH50	63-125	0.416720	0.620382	2.5 Y 7/1	none
CH62	63-125	0.236580	0.480777	2.5 Y 7/2	none
CH77	63-125	0.215370	0.435339	10 YR 6/2	Gt
CH80	63-125	0.228852	0.444792	10 YR 7/2	Gt
CH81	63-125	0.224573	0.434804	10 YR 6/3	Gt
CH82	63-125	0.229609	0.426331	10 YR 6/2	none
CH02	125-2000	0.205918	0.414482	10 YR 6/3	Gt
CH08	125-2000	0.242425	0.351896	10 YR 7/1	none
CH09	125-2000	0.342392	0.468819	2.5 Y 7/2	none
CH11	125-2000	0.231675	0.374852	7.5 YR 6/1	none
CH23	125-2000	0.264845	0.564345	2.5 Y 7/2	none
CH24	125-2000	0.275900	0.411181	5 Y 7/1	none
CH25	125-2000	0.351894	0.572138	5 Y 7/1	none
CH26	125-2000	0.312031	0.465523	2.5 Y 7/1	none
CH50	125-2000	0.347974	0.509715	10 YR 8/1	none
CH62	125-2000	0.235294	0.439320	2.5 Y 7/2	none
CH77	125-2000	0.287378	0.435116	2.5 Y 6/2	none
CH80	125-2000	0.271521	0.439451	2.5 Y 7/1	none
CH81	125-2000	0.258054	0.413808	2.5 Y 7/1	none
CH82	125-2000	0.266490	0.441001	2.5 Y 7/2	none
CH23ped	ped	0.195348	0.451272		Gt
CH23ped2	ped	0.352285	0.690805	2.5 Y 7/2	none
CH23pedb	ped	0.384462	0.690775	2.5 Y 7/2	none
CH24ped	ped	0.372865	0.537593	5 Y 7/1	none
CH25ped	ped	0.396551	0.541394	2.5 Y 8/1	none
CH50ped	ped	0.555384	0.709432	5 Y 8/1	none
CH62ped	ped	0.389932	0.564355	2.5 Y 8/1	none

Average total reflectance (ATR) is average reflectance over entire wavelength range (0.35 to 2.50 µm) and average visible reflectance (AVR) is average reflectance over visible wavelengths (0.40 to 0.70 µm); Gt=goethite; Ht=hematite; RS=mineral identification from reflectance spectra.

Table S2. Magnetic Hysteresis Properties and Susceptibility for Bodélé Surface Sediments.

Sample #	Particle Size (μm)	M_s (Am^2/kg)	M_r (Am^2/kg)	H_c (mT)	H_{cr} (mT)	σ_{hys}	χ_{hf} (m^3/kg)	χ_{lf} (m^3/kg)	χ_{fd} (m^3/kg)
CH02	< 63	3.237E-02	5.538E-03	11.31	31.78	0.235	3.086E-08	3.127E-07	9.173E-09
CH08	< 63	1.692E-02	3.445E-03	13.67	39.04	0.312	2.801E-08	2.126E-07	7.099E-09
CH11	< 63	1.528E-02	3.552E-03	14.92	41.82	0.307	3.114E-08	1.894E-07	5.965E-09
CH23	< 63	5.052E-03	7.528E-04	6.37	24.93	-0.453	4.599E-08	9.775E-08	4.094E-10
CH24	< 63	2.159E-03	3.958E-04	13.05	32.51	-0.399	8.738E-08	1.015E-07	6.998E-10
CH39	< 63	5.196E-01	9.589E-02	10.38	22.61	-0.021	1.225E-07	5.316E-06	8.670E-08
CH62	< 63	4.436E-03	7.518E-04	16.54	39.61	-0.436	1.021E-07	1.412E-07	2.090E-09
CH80	< 63	2.891E-02	5.482E-03	12.97	39.20	0.277	5.120E-08	3.362E-07	9.144E-09
CH81	< 63	2.176E-02	3.989E-03	12.85	38.62	0.279	4.723E-08	2.556E-07	7.241E-09
CH08	125-2000	1.842E-03	2.590E-04	9.48	21.57	-0.282	5.919E-08	7.962E-08	7.996E-10
CH11	125-2000	3.595E-03	5.701E-04	11.75	31.56	-0.396	8.369E-08	1.143E-07	2.086E-09
CH80	125-2000	2.408E-03	4.406E-04	11.77	31.66	-0.220	7.141E-08	9.065E-08	6.209E-10
CH81	125-2000	2.809E-03	6.205E-04	12.53	31.50	-0.394	8.571E-08	1.102E-07	1.862E-09

M_s =saturation magnetization; M_r =saturation remanent magnetization; H_c =coercivity; H_{cr} =coercivity of remanence; σ_{hys} =hysteresis loop shape parameter; χ_{hf} =high-field magnetic susceptibility from hysteresis loop; χ_{lf} =low-field AC susceptibility in 1 Hz; χ_{fd} =frequency dependent susceptibility.

Table S3. Magnetic Remanence and Chemical Properties for Bodélé Surface Sediments.

Sample #	Particle Size (µm)	Total Fe (ppm)	SIRM	HIRM	M _{Ht}	M _{Gt}	S ₃₀₀	FeOx	%Fe Magnetite	Silicate
					(x10 ⁻⁵ Am ² /kg)					
CH02 HM	< 63	18,000	553.8	45.69	68.31	68.61	0.83	61.11%	1.41%	37.47%
CH08 HM	< 63	17,000	344.5	42.32	50.41	71.96	0.76	57.83%	0.78%	41.39%
CH11 HM	< 63	15,000	355.2	38.80	42.28	59.39	0.93	54.45%	0.80%	44.75%
CH23 LM	< 63	18,000	48.80	2.27	2.35	0.83	0.88	1.42%	0.22%	98.36%
CH24 LM	< 63	32,000	33.81	1.69	3.31	0.47	0.90	0.95%	0.05%	99.00%
CH25 LM	< 63		36.25	2.03			0.86			
CH26 LM	< 63		71.41	2.56			0.89			
CH39	< 63	54,000	9358	114.2	190.0	23.95	0.97	37.96%	7.57%	54.47%
CH50 LM	< 63		13.51	0.32			0.95			
CH62 LM	< 63	37,000	65.29	2.95	7.13	0.88	0.95	1.74%	0.09%	98.17%
CH80 HM	< 63	25,000	548.2	48.64	64.56	66.80	0.81	42.21%	0.91%	56.88%
CH81 HM	< 63	23,000	398.9	41.35	51.57	63.33	0.78	40.14%	0.74%	59.12%
HM Mean		19,600	440.1	43.36	55.43	66.02	0.82	51.4%	0.93%	47.92%
LM Mean		29,000	49.30	2.30	4.26	0.73	0.91	1.37%	0.12%	98.5%
Mean (All)		26,556	985.6	28.57	53.32	39.58	0.88	33.1%	1.4%	65.5%
CH02 HM	63-125		58.23	12.11			0.58			
CH08 HM	63-125		54.26	10.99			0.59			
CH09 HM	63-125		57.55	0.61			0.98			
CH11 HM	63-125		67.65	12.97			0.62			
CH23 LM	63-125		26.89	0.72			0.95			
CH24 LM	63-125		30.87	1.74			0.89			
CH25 LM	63-125		39.83	2.71			0.86			
CH26 HM	63-125		73.54	2.34			0.94			
CH39	63-125		7321	80.28			0.98			
CH50 LM	63-125		14.93	0.11			0.99			
CH62 LM	63-125		45.08	2.81			0.88			
CH77 HM	63-125		55.37	11.12			0.60			
CH80 HM	63-125		69.88	13.53			0.61			
CH81 HM	63-125		50.09	10.62			0.58			
CH82 HM	63-125		50.62	8.61			0.66			
HM Mean			59.69	9.21			0.68			
LM Mean			31.52	1.62			0.91			
Mean(All)			534.39	11.42			0.78			
CH02 HM	125-2000		11.64	3.72			0.36			
CH08 HM	125-2000		32.36	2.27			0.86			
CH09 HM	125-2000		47.92	2.33			0.90			
CH11 HM	125-2000		44.90	3.08			0.86			
CH23 LM	125-2000		14.47	0.83			0.88			
CH24 LM	125-2000		25.98	1.70			0.87			
CH25 LM	125-2000		33.41	1.65			0.90			
CH26 HM	125-2000		72.50	2.72			0.93			
CH50 LM	125-2000		9.91	0.50			0.90			
CH62 LM	125-2000		40.26	2.55			0.87			
CH77 HM	125-2000		39.64	2.37			0.88			
CH80 HM	125-2000		44.71	3.10			0.86			
CH81 HM	125-2000		42.89	2.56			0.88			
CH82 HM	125-2000		46.81	2.31			0.90			
HM Mean			42.60	2.72			0.83			
LM Mean			24.81	1.45			0.88			
Mean (All)			36.24	2.26			0.85			

SIRM=isothermal remanent magnetization; HIRM=hard IRM; $S_{300}=(IRM_{-0.3T})/IRM_{1T}$, lower values indicating higher ferric oxide amounts relative to ferrimagnetic minerals; M_{Ht} and M_{Gt} are the hematite and goethite remanent magnetizations obtained from the Carter-Guyodo method; HM=high magnetization sample group; LM=low magnetization sample group; % total Fe occurring as ferric oxides (FeOx), magnetite, and ferric silicates determined from equation (1) in text or directly from magnetization and Mössbauer spectroscopy for CH39. The mean magnetization values for all samples is heavily biased by sample CH39.

Table S4. Mössbauer Parameters at 300 K and 4.2 K for Bodélé Surface Sediments

Sample	Phase	B _{Hf} (T)	QS (mm/s)	IS (mm/s)	%	B _{Hf} (T)	QS (mm/s)	IS (mm/s)	%
<i>T=300 K</i>						<i>T=4.2K</i>			
CH02	Ht	50.6	-0.21	0.37	19	52.8	-0.19	0.53	24
	Gt	nd				49.5	-0.26	0.52	37
	Fe ³⁺		0.61	0.38	81		0.60	0.46	39
CH24	Ht	nd				nd			
	Gt	nd				nd			
	Fe ³⁺		0.50	0.37	100		0.54	0.46	100
CH62	Ht	nd				nd			
	Gt	nd				nd			
	Fe ³⁺		0.55	0.37	100		0.60	0.46	100
CH39	Ht	49.8	-0.15	0.38	19	52.5	-0.12	0.51	24
	Gt	nd				49	-0.14	0.48	14
	Fe ³⁺		0.64	0.36	69		0.64	0.49	53
	Fe ²⁺		2.36	1.1	12		2.21	1.54	9

Hyperfine field (B_{hf}), quadrupole splitting (QS), isomer shift (IS), and relative proportion of subspectrum to total area (%). MB parameter uncertainties are ± 0.01 mm/s for IS and QS, ± 0.1 T for B_{hf}, and $\pm 5\%$ for spectral areas. B_{hf} is the mean value of the hyperfine field distribution (HFD). Fe³⁺ and Fe²⁺ parameters reflect paramagnetic phases having overlapping doubles with a variety of Fe silicate minerals and/or nanophase (superparamagnetic) ferric oxide at 300 K, nd= did not detect. QS for hematite at 4.2 K was negative in all samples. This is typical for hematite above its Morin transition where it is in a weakly ferromagnetic state. In the antiferromagnetic state ($T < T_m$) QS is positive

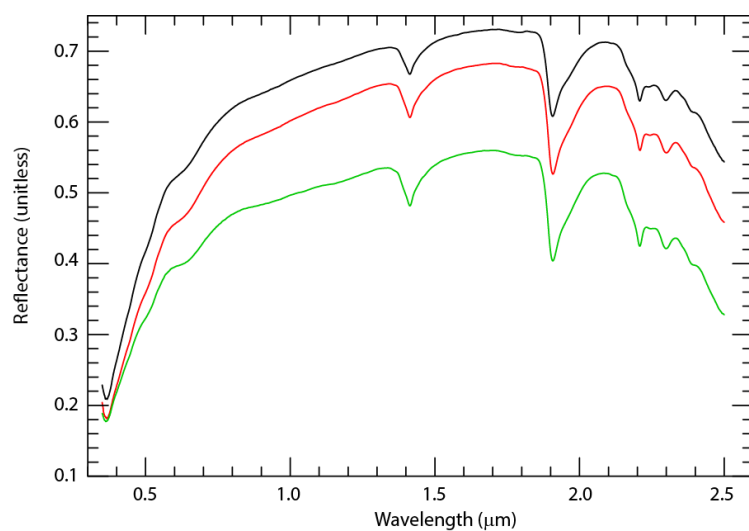


Figure S1 Reflectance spectra across solar radiation spectrum (wavelength range from 0.35 to 2.50 micrometer) for sample CH26. Spectra measured for three different particle size fractions: fine (PM63, < 63μm, black line), medium (63-125μm, red line), and coarse (125-2000μm, green line).

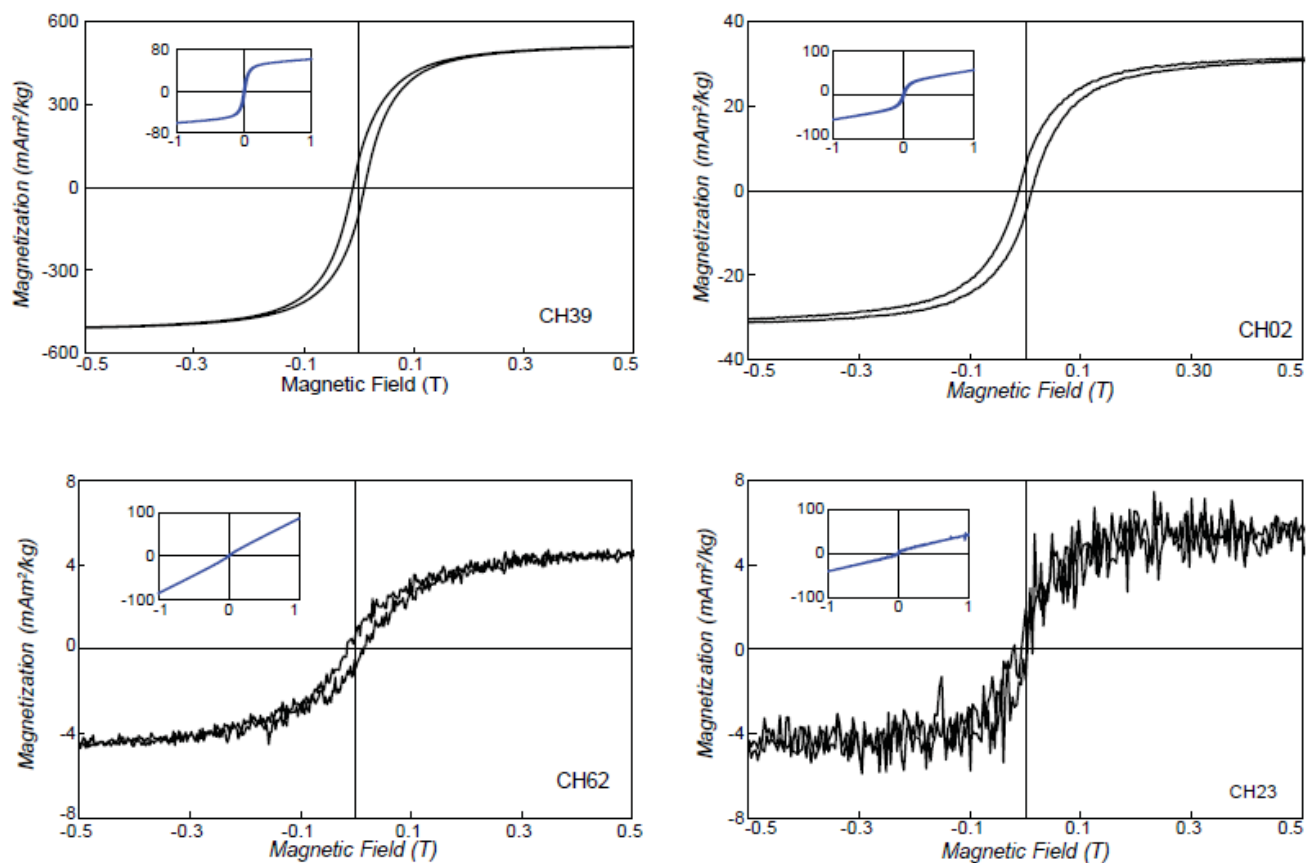


Figure S2: Representative hysteresis loops for Bodélé surface sediments (CH39, CH02, CH62, and CH23). The main plots are slope corrected for paramagnetic effects and are expanded views of the loops for magnetic fields ± 0.5 T. The insets are the full (± 1 T) uncorrected loops. The magnetization axis is in mass normalized units of 10^{-3} Ampere-meter²/kg (mAm^2/kg).

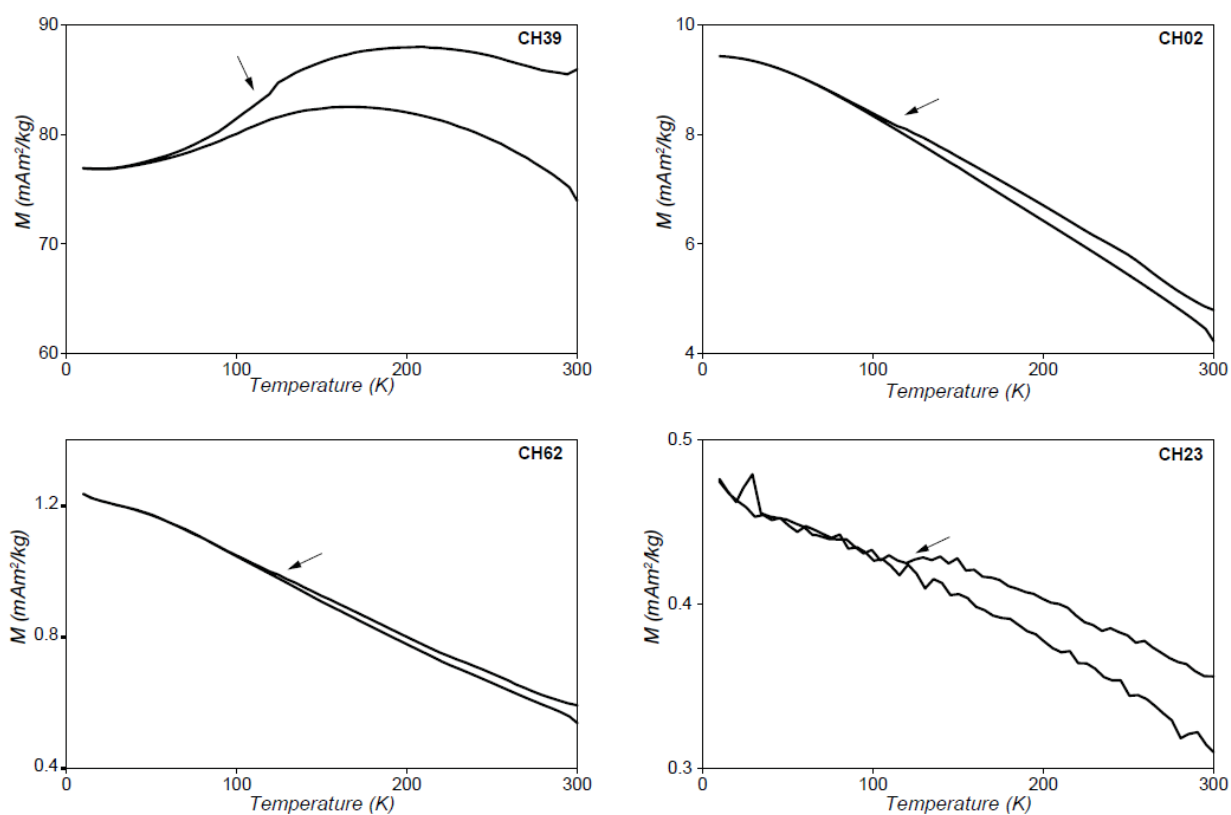


Figure S3. Low-temperature magnetization cooling and warming curves (RTSIRM). Initial remanence is given in a 2.5 T field at 300 K and measurements are collected in zero-field during 300K to 10K to 300K thermal cycling. The drop in magnetization near 100 K denoted by arrows indicate possible Verwey transition due to magnetite. The magnetization axis is in mass normalized units of 10^{-3} Ampere-meter²/kg ($\text{mA}\cdot\text{m}^2/\text{kg}$). Low magnetization (LM) group: CH62 and CH23; High magnetization (HM) group: CH02; Angamma Delta sediments: CH39

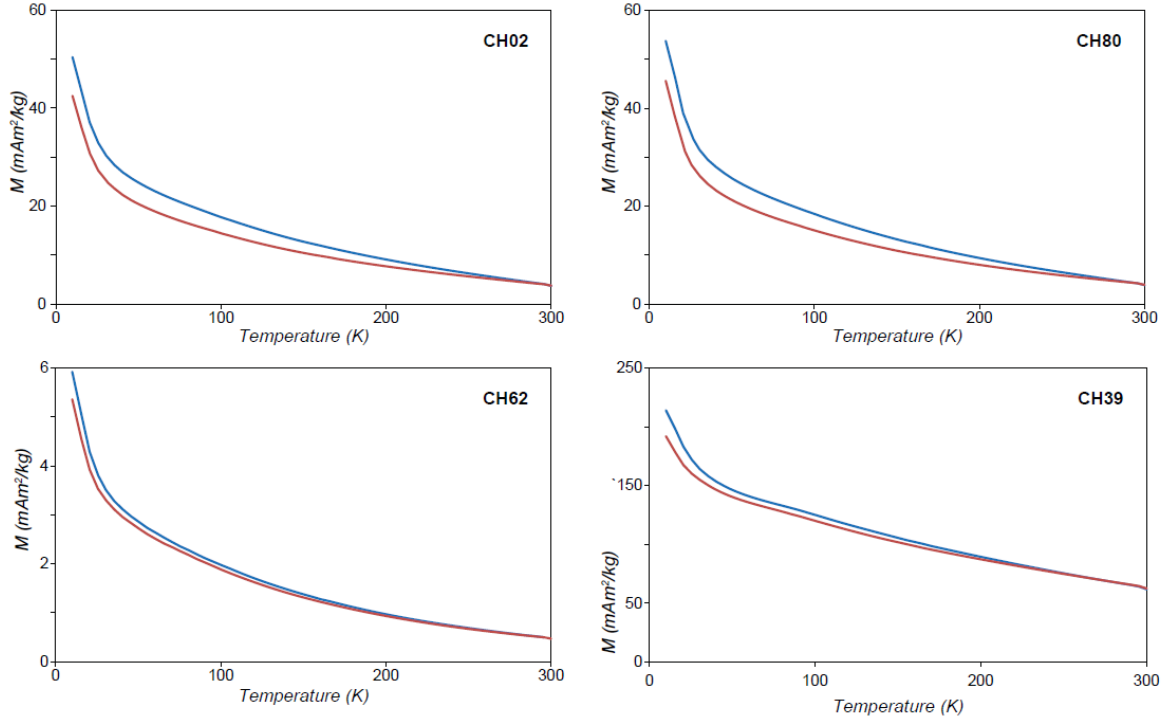


Figure S4. Low-temperature field cooled (FC) and zero-field cooled (ZFC) curves. Measurements are collected in zero-field on warming to 300 K (FC=blue lines, ZFC=red lines). Larger FC-ZFC offsets are observed for HM samples (CH02, CH80) than for LM sample (CH62). The slight inflection near $T=100$ K for CH39 is due to the Verwey Transition in magnetite.

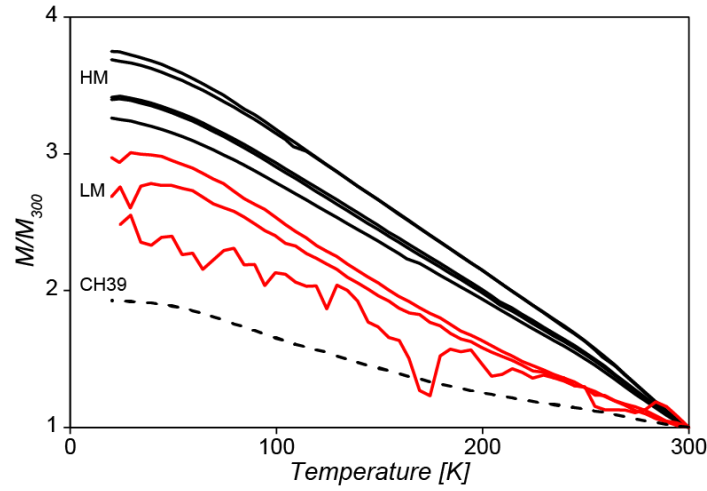


Figure S5: Normalized temperature variation of remanence highlighting the goethite contribution to remanence. Magnetization is acquired by cooling from 400 to 300 K in a 2.5 T field and then partially demagnetized in 0.2 T alternating field (AF) at 300 K (Carter-Guyodo method). Black lines are samples in the high magnetization (HM) group, red lines are samples in the low magnetization (LM) group, and dashed-line is CH39. Remanence curves are measured during zero-field cooling from 300 to 20 K followed by zero-field warming back to 300 K. Curves are normalized by the remanence value at 300 K after AF demagnetization. Low temperature remanence ratio, $R_{LT} = M(10 \text{ K})/M(300 \text{ K})$; RLT ratios greater than 2.0 are diagnostic for goethite.

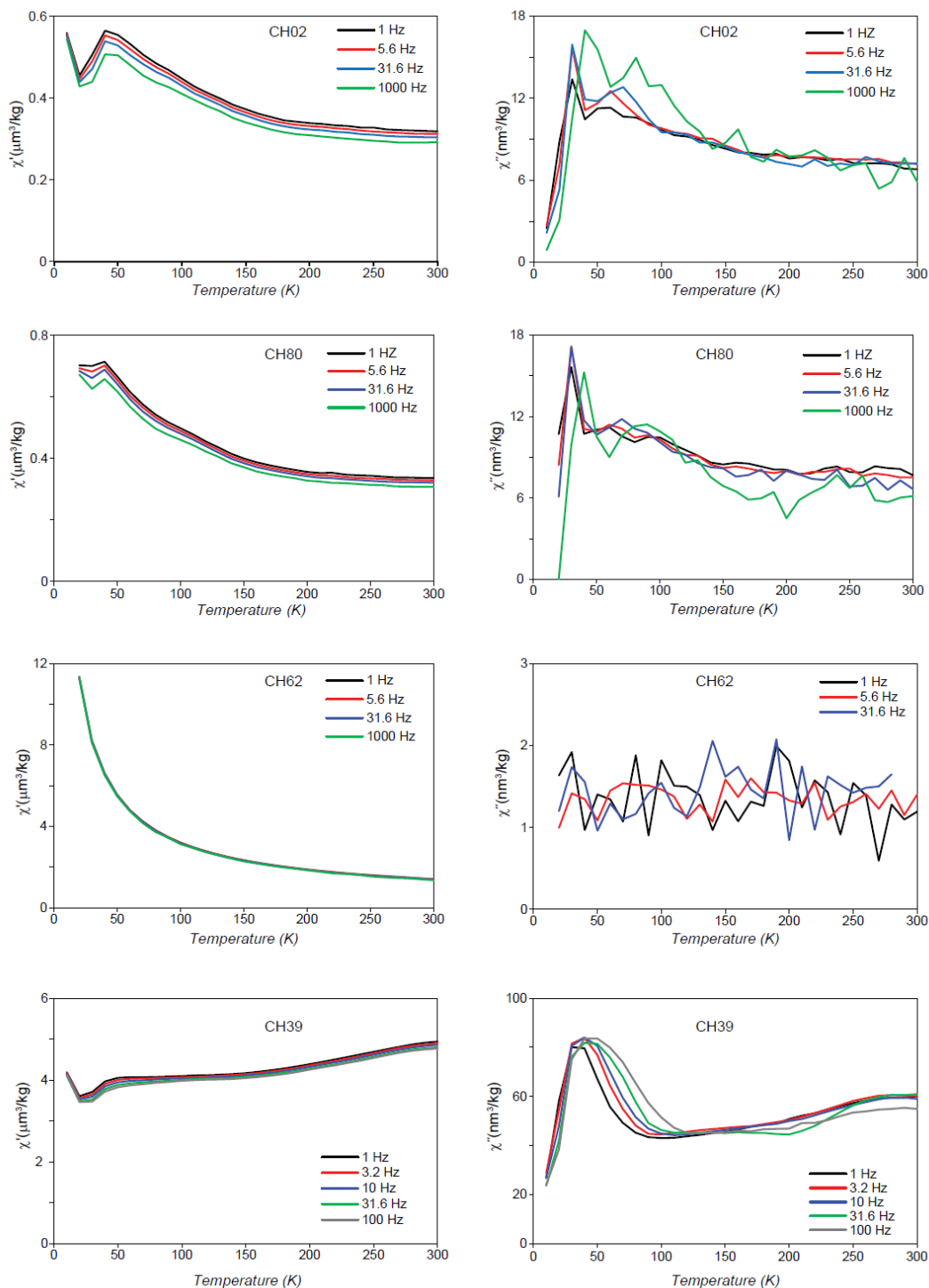


Figure S6: In-phase (χ') and quadrature (χ'') susceptibility at variable frequencies measured from 10 K to 300 K. The left-side panel is in-phase susceptibility in units of $10^{-6} \text{ m}^3/\text{kg}$ ($\mu\text{m}^3/\text{kg}$) and the right-side panel is quadrature susceptibility in units of $10^{-9} \text{ m}^3/\text{kg}$ (nm^3/kg). Strong frequency dependence and non-zero quadrature susceptibility for CH02, CH80, and CH39 over the whole temperature range indicates a broad size distribution of nanoparticles. CH62 displays paramagnetic behavior with no frequency dependence and

near zero quadrature susceptibility. Low magnetization (LM) group: CH62; High magnetization (HM) group: CH02 and CH80; Angamma Delta sediments: CH39.

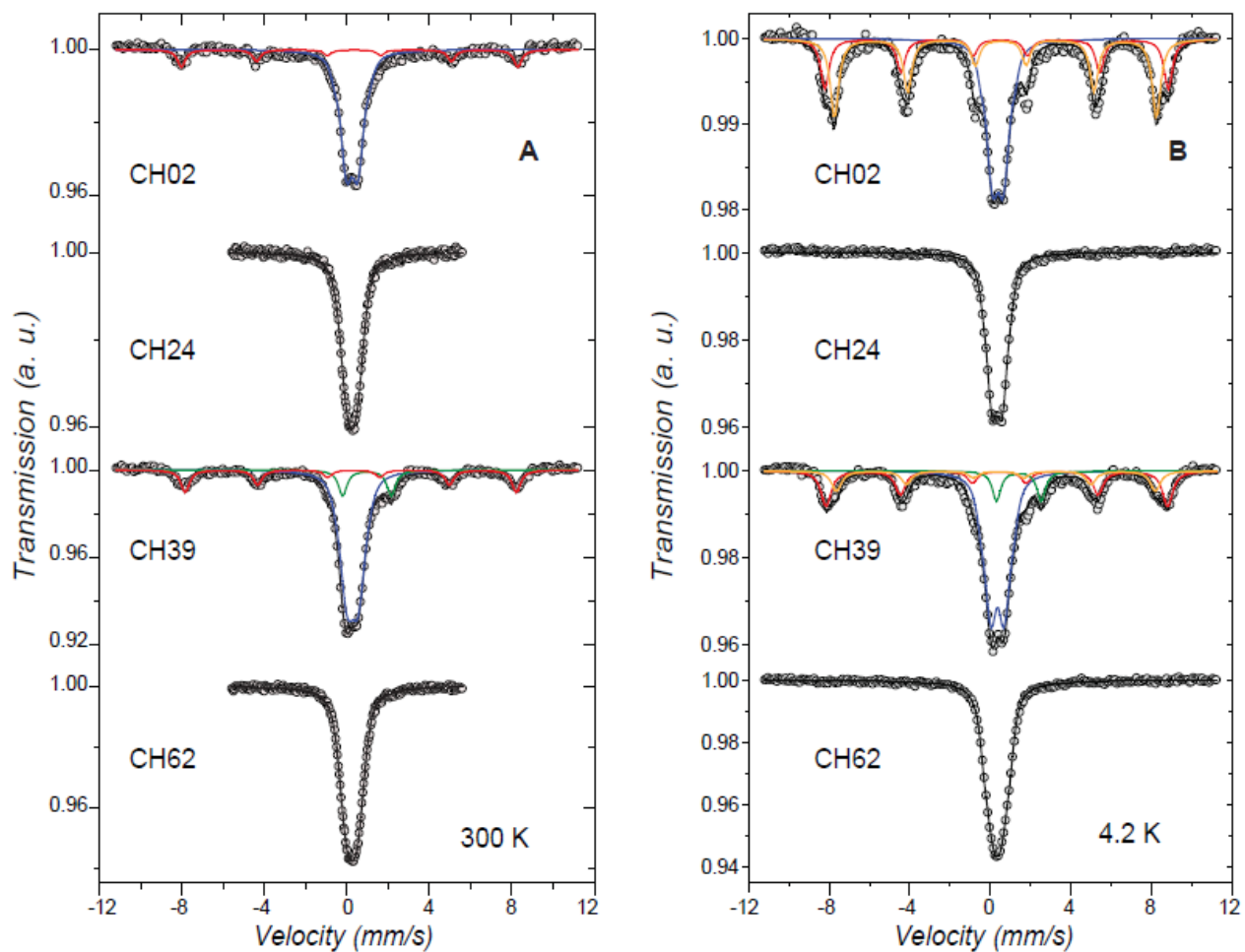


Figure S7: Mössbauer Spectra at 300 K (a) and 4.2 K (b). Open circles are experimental data and black line is best total fit using components represented by hematite (red), goethite (orange), Fe^{3+} (blue), and Fe^{2+} (green). Room-temperature spectra are dominated by a central doublet corresponding to ferric paramagnetic silicate minerals and/or nanophase ferric oxides. Low magnetization (LM) group: CH62 and CH24; High magnetization (HM) group: CH02; Angamma Delta sediments: CH39

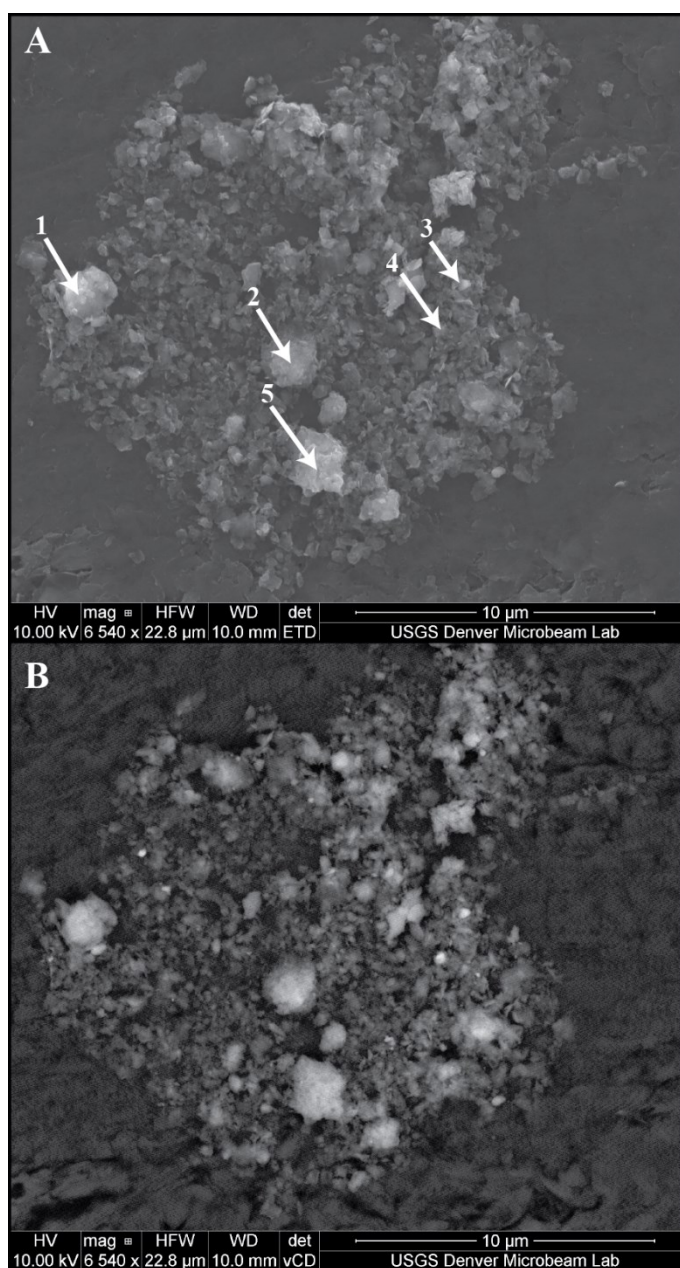


Figure S8. Scanning electron micrograph of a composite grain in sample CH-77. (a) Secondary electron image. Areas 1 and 2, smectitic clays having <5 wt. % Fe; area 3, iron oxide nanoparticle (brightest speck, ~25 wt. % Fe) on clay mineral; area 4, apatite particle about 200 nm across and clay having about 8 wt. % Fe; area 5, silica grain with clay mineral having <5 wt. % Fe. (b) Backscatter electron micrograph.